THESIS FOR THE DEGREE OF DOCTOR OF PHILOSOPHY IN THERMO AND FLUID DYNAMICS

Aerodynamic design framework for low-pressure compression systems

MARCUS LEJON

Department of Mechanics and Maritime Sciences
Division of Fluid Dynamics
CHALMERS UNIVERSITY OF TECHNOLOGY

Gothenburg, Sweden 2018

Aerodynamic design framework for low-pressure compression systems
MARCUS LEJON
ISBN 978-91-7597-759-1

© MARCUS LEJON, 2018

Doktorsavhandlingar vid Chalmers tekniska högskola
Ny serie nr. 4440
ISSN 0346-718X
Department of Mechanics and Maritime Sciences
Division of Fluid Dynamics
Chalmers University of Technology
SE-412 96 Gothenburg
Sweden
Telephone: +46 (0)31-772 1000

Cover:
Geometry of the low-pressure compression system designed in Section 5 in this thesis. Static pressure contours for a single blade passage are shown.

Chalmers Reproservice
Gothenburg, Sweden 2018

Aerodynamic design framework for low-pressure compression systems
Thesis for the degree of Doctor of Philosophy in Thermo and Fluid Dynamics
MARCUS LEJON
Department of Mechanics and Maritime Sciences
Division of Fluid Dynamics
Chalmers University of Technology

ABSTRACT

Aircraft engine manufacturers strive to improve current state of the art designs through continuous development efforts. By improving existing designs and exploring new alternatives, the goal is to reduce the fuel consumption - a topic of high relevance due to the remarkable growth rate of air traffic. To achieve a low fuel consumption, turbofan engines should operate at a high overall pressure ratio which is commonly achieved by an axial compressor. An axial compressor consists of a set of consecutive stages, each consisting of a rotating and stationary blade row. While a compressor should operate with a high pressure ratio, it should not operate too close to its stability limit where surge can occur. If surge occur in the compressor, the compressor blades will be subject to large transient forces and the flow may even reverse direction. The main focus of this thesis is the further development of an aerodynamic design framework for low-pressure systems, where an appropriate level of modeling is selected and compressor stages are optimized with respect to efficiency and stability. Different approaches are used to evaluate stability of a compressor stage and it is concluded that the static pressure rise capability of the stage is an appropriate measure to use for ranking designs in an optimization. As a part of this thesis, all three stages of a three-stage compressor are optimized using steady state RANS calculations, and the performance of the three-stage compressor is evaluated as an assembly. The possibility of replacing blade geometries to improve part- or design speed stability of the three-stage compressor is shown. Other aspects which may penalize efficiency are investigated, namely the influence of surface roughness and manufacturing variations on performance. The influence of surface roughness on optimal stage designs is assessed by optimizing compressor blades with and without taking surface roughness into account. The impact of manufacturing variations on performance at a design point is investigated by utilizing measurements of a manufactured compressor blisk.

Keywords: Turbomachinery, compressor, CFD, tip clearance, validation, optimization, manufacturing variations, surface roughness, stage matching

List of publications

This thesis is based on the work contained in the following publications:

I M. Lejon, L-E. Eriksson, N. Andersson and L. Ellbrant, 2015, Simulation of Tip-Clearance Effects in a Transonic Compressor, *Proceedings of ASME Turbo Expo 2015*, June 15–19, Montréal, Canada

II M. Lejon, N. Andersson, L. Ellbrant and H. Mårtensson, 2015, CFD Optimization of a Transonic Compressor Stage with a Large Tip Gap, *22nd ISABE Conference*, October 25–30, Phoenix, USA

III M. Lejon, N. Andersson, T. Grönstedt, L. Ellbrant and H. Mårtensson, 2016, Optimization of Robust Transonic Compressor Blades, *Proceedings of ASME Turbo Expo 2016*, June 13–17, Seoul, South Korea

IV M. Lejon, T. Grönstedt, N. Glodic, P. Petrie-Repar, M. Genrup, A. Mann, 2017, Multidisciplinary Design of a Three-Stage High Speed Booster, *Proceedings of ASME Turbo Expo 2017*, June 26–30, Charlotte, USA

V M. Lejon, N. Andersson, T. Grönstedt, L. Ellbrant and H. Mårtensson, 2017, On Improving the Surge Margin of a Tip-Critical Axial Compressor Rotor, *Proceedings of ASME Turbo Expo 2017*, June 26–30, Charlotte, USA

VI M. Lejon, N. Andersson, L. Ellbrant and H. Mårtensson, 2017, The Surge Margin of an Axial Compressor: Estimations from Steady State Simulations, *23rd ISABE Conference*, September 3–8, Manchester, UK

Accepted for publication:

VII M. Lejon, N. Andersson, L. Ellbrant and H. Mårtensson, 2018, The Impact of Manufacturing Variations on Performance of a Transonic Axial Compressor Rotor, *Proceedings of ASME Turbo Expo 2018*, June 11–15, Oslo, Norway

ACKNOWLEDGEMENTS

I would first and foremost like to thank my family for being supportive throughout this endevour. I would also like to thank my fiancée Linda for her support, patience, and for bringing me so much joy.

I would like to thank Hans Mårtensson and Lars Ellbrant at GKN Aerospace Engine Systems in Trollhättan for sharing their expertise and for encouraging me during these years. Their support has been tremendously valuable. I would also like to thank my supervisor at Chalmers Niklas Andersson for supporting me in this undertaking, and always taking the time to discuss and provide feedback on my work. Furthermore, I would like to thank Lars-Erik Eriksson, my supervisor at the outset of this work who is now retired. He was the one who first described the topic of the thesis to me when I was doing my master thesis. He made me interested in the subject and I subsequently applied for the PhD position. We had many interesting discussions on compressor aerodynamics, and his pedagogical approach helped me gain many insights.

Thank you to my friends and colleagues at Chalmers for making it a great place to work. For the complete duration of my PhD studies I have shared my office at Chalmers with Alexandre Capitao Patrao, who has been a great friend. We took the opportunity, when we got the chance, to travel and explore parts of the west coast of the US. A great memory. I would also like to thank my friends and colleagues at GKN Aerospace Engine Systems in Trollhättan. I'm fortunate to have found good friends at my work place, a place where I will now be spending more time at as one chapter draws to a close, and a new one begins.

This work was funded by the Swedish National Aviation Engineering Research Programme, NFFP. The author would like to acknowledge the financial support of VINNOVA, the Swedish Defence Material Administration (FMV) and GKN Aerospace. The author would also like to thank the National Supercomputer Center, Linköping, Sweden, and Chalmers Centre for Computational Science and Engineering, Gothenburg, Sweden, for the computational resources required for this work.

To Linda

NOMENCLATURE

B	Constant used in law of the wall
ΔB	Shift of the law of the wall
C	Flow velocity
C_p	Static pressure recovery coefficient, specific heat at constant pressure
C_v	Specific heat at constant volume
$\mathcal{F}$	Flux vector
$\mathcal{H}$	Source vector
$\dot{m}$	Mass flow
N	Rotational speed
P, p	Pressure
P_k	Turbulence production
Q	State vector
R	Roughness, gas constant
S	Strain rate tensor
T	Temperature
U	Blade speed
ϵ	Sand grain roughness parameter conversion factor, turbulence dissipation, model constant
η_p	Polytropic efficiency
γ	Ratio of specific heats
k	Turbulence kinetic energy
k_s	Sand grain roughness
k_s^+	Sand grain roughness Reynolds number
κ	von Karman constant
μ	Dynamic viscosity
μ_t	Turbulence viscosity
ν	Kinematic viscosity
ϕ	Flow coefficient
ρ	Density
τ_w	Wall shear stress
u_*	Friction velocity
u	Velocity
t	Time step
y	Wall distance
y^+	non-dimensional wall distance

Subscripts

0	Total condition

1	Rotor inlet
2	Rotor outlet/stator inlet
3	Stator outlet
a	Average
q	Root mean square
r	Rotor
ref	Reference
rel	Relative
$corr$	Corrected
s	Stator
TT	Total-to-total
t	Turbulence
x	Axial

Abbreviations

CFD	Computational fluid dynamics
FOD	Foreign object damage
GA	Genetic Algorithm
LHS	Latin hypercube sampling
PCA	Principal component analysis
PR	Pressure ratio
R	Rotor
RBF	Radial basis function
SM	Surge margin
S	Stator

Contents

Abstract i

List of publications iii

Acknowledgements v

Nomenclature ix

Contents xi

1 Introduction 1

1.1 Motivation 1

1.2 Scope of work 4

2 Design 5

2.1 Requirements 5

2.1.1 Surge margin 5

2.1.2 Efficiency 7

2.2 Multi-stage considerations 7

3 CFD Modeling 9

3.1 Governing equations 9

3.2 Discretization 11

3.3 Computational grid 11

3.3.1 Grid sensitivity 12

3.4 Boundary conditions 14

3.4.1 Wall modeling 15

3.5 Geometric representation 16

3.5.1 Tip clearance 16

3.5.2 Surface roughness 19

3.5.3 Manufacturing variations 24

3.6 Turbulence model 26

4 Optimization procedure 29

4.1 Optimization algorithm 29

4.2 Optimization framework 30

4.3 Meta model 32

4.4 Lipschitz sampling 33

5 Re-design of a low-pressure compression system 35
5.1 Design of a three-stage axial compressor 35
5.1.1 Methodology 35
5.1.2 Computational setup 36
5.1.3 Results 37
5.2 Transonic fan re-designed 44
5.3 Complete low-pressure compression system 46

6 Summary of Papers 47
6.1 Paper I 47
6.1.1 Division of work 47
6.1.2 Summary and discussion 47
6.2 Paper II 48
6.2.1 Division of work 48
6.2.2 Summary and discussion 48
6.3 Paper III 48
6.3.1 Division of work 49
6.3.2 Summary and discussion 49
6.4 Paper IV 49
6.4.1 Division of work 50
6.4.2 Summary and discussion 50
6.5 Paper V 50
6.5.1 Division of work 50
6.5.2 Summary and discussion 51
6.6 Paper VI 51
6.6.1 Division of work 51
6.6.2 Summary and discussion 51
6.7 Paper VII 52
6.7.1 Division of work 52
6.7.2 Summary and discussion 52

7 Concluding remarks 53
7.1 Stability 53
7.2 Multi-stage optimization 54
7.3 Surface roughness and manufacturing variations 54
7.4 Future work 55

Bibliography 57

1 Introduction

1.1 Motivation

The demand for flight is increasing as more people travel the world and as more cargo is transported by flight. Historic data from 1995-2012 show that the current growth of air traffic (total number of kilometers traveled by passengers) results in air traffic being doubled every 15th year [1]. This large growth in air traffic results in a high demand for fuel efficient aircraft engines to keep the fuel consumption and emissions as low as possible. Fortunately, historic data compiled from 1971–2015 shows that the increase in fuel consumption has not been as high as the increase in air traffic. Rather, the fuel consumption has been reported to double every 34 years (average increase of 2.1% per year [2]). The difference in air traffic growth and the increase in fuel consumption highlights the success and importance of continuous development of aircraft and engine systems. In 2008, a large number of airlines, aircraft manufacturers, engine manufacturerers and airports committed to the Air Transport Action Group (ATAG) CO2 emission goals [3], which state that the net carbon emission from aviation in 2050 should be half of what it was in 2005. Four key areas are highlighted as important to achieve the reduction in CO2: technology, improved operational practises, infrastructure improvements and economic measures. Out of these areas, technology is identified in [3] as the area which ”has by far the best prospects for reducing aviation emissions”. Existing technology must be improved and new technology as well as biofuels needs to be introduced.

The most frequently used engine design for passenger transport is the turbofan engine, illustrated in Figure 1.1.1, where the main portion of the air flow that pass through the fan at the front of the engine bypass the engine core, while a smaller portion of the air flow enter the engine core and is further compressed and used for combustion. The ratio

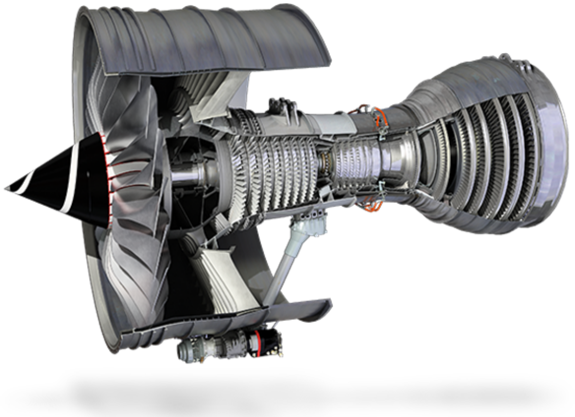

Figure 1.1.1: *Rolls-Royce Trent 900 turbofan engine [4]. Used with permission.*

of air mass flow that bypass the engine core relative to the air mass flow entering the engine core is called the bypass ratio. For a turbofan engine, a high bypass ratio is one key parameter to reduce the specific fuel consumption (fuel consumption per unit of thrust) and a state of the art modern turbofan engine can have a bypass ratio of 12:1 [5]. Other key parameters are the turbine inlet temperature, the pressure ratio of the fan and the overall pressure ratio. Engine weight and losses are influenced by the selection of these parameters and an optimization needs to be made to find a design with low specific fuel consumption. The overall pressure ratio is achieved by the compression system, and can be in the range 40-50 for a modern turbofan engine [6]. Two types of compressors are used in turbofan engines: centrifugal (radial) and axial compressors, with the latter being the most commonly used type in modern large turbofan engines. Advantageous of the axial compressor is the potential to higher pressure ratios and higher mass flow rates for a given frontal area compared to the centrifugal compressor. A disadvantage is that the blade height is reduced further back in the axial compressor, which may give rise to higher losses due to the increased relative size of tip clearances, discussed more in *Section* 3.5.1. Advantageous of the centrifugal compressor include the ability to operate at low flow rates and to operate over a wider range of mass flows for a given rotational speed. Moreover, a centrifugal compressor has a better resistance to foreign object damage (FOD) [7].

An axial compressor is made up of stages of rotating and stationary blades called rotors and stators, respectively. As the aviation industry strive towards lighter engines, it is desirable to achieve high pressure ratios across each stage of the compressor to keep the number of stages to a minimum. The desire to achieve a high pressure ratio across each stage is challenging from a design perspective as increasing the blade loading can penalize efficiency and require operating the compressor closer to its stability limit.

The performance curve of the compressor at a constant rotational speed is called a speedline, illustrated in Fig. 1.1.2 at four different rotational speeds. The higher end of the mass flow range along a speedline is limited by choke, where the velocity of the flow is equal to the speed of sound (Mach number equal to 1) across the blade from hub to casing. If the back pressure is gradually increased from a choked operating condition, the mass flow eventually decrease as the compressor becomes un-choked, and the pressure ratio across the compressor rise. At some mass flow rate, the flow in one or several blade passages separate, the blades have stalled. It may be a part-span stall or a region of separated flow may cover the entire span. Although not desirable, it may be possible for the compressor to still operate with stall in one or several of the first stages as reported in [7]. Stall may lead to surge, where the compressor goes from an un-stalled state, to stalled and back to un-stalled in a transient process [8]. During surge, the mass flow through the compressor change in time and the process may even lead to flow reversal. Surge is a dangerous state as the blades are subject to large transient forces and, in an engine setup, hot gases from combustion could flow back into the compressor causing damage.

The operating line, illustrated in the compressor map in Fig. 1.1.2, is the performance curve that the compressor is designed to operate along as the rotational speed of the compressor is varied. A line, called the surge line, can be drawn through the last stable operating point at the lower end of the mass flow range for a number of rotational speeds. Due to the adverse impact of surge on performance and the danger of damaging the engine, it is important to have a safety margin from the operating line of the compressor to the surge line at all rotational speeds, usually called a stall or surge margin. The surge margin of the compressor should be sufficiently high to ensure safe operation. If the surge margin is too low, variations of the incoming flow field, or rapid changes of the rotational speed may cause the compressor to surge. High efficiency and a sufficiently high surge margin to ensure a stable operating condition along the entire operating line of the compressor are thus desirable traits which should be considered at the beginning of the design process of a compressor.

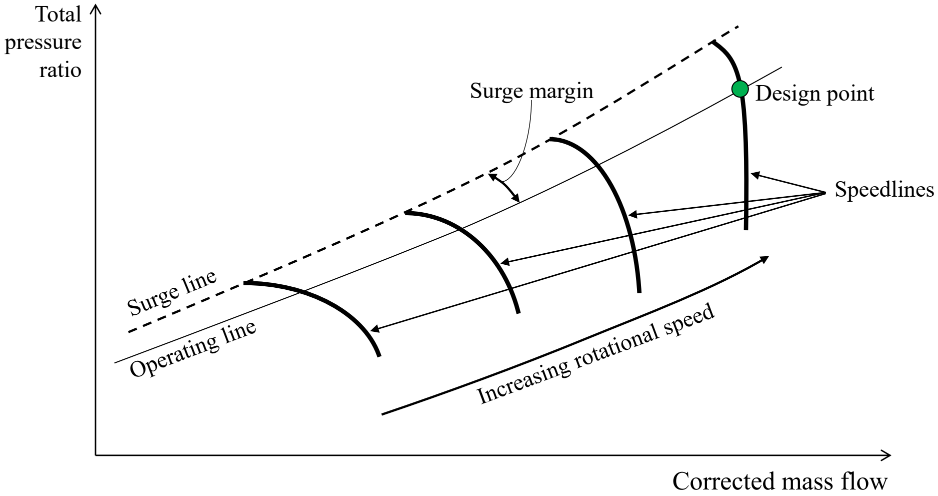
Total pressure ratio
Surge margin
Design point
Speedlines
Surge line
Operating line
Increasing rotational speed
Corrected mass flow

Figure 1.1.2: *Compressor map*

1.2 Scope of work

The work presented in this thesis focus on the design methodology of a compressor with respect to efficiency and stability using 3D CFD calculations. The work can be divided into the three main topics listed below.

Selection of optimization criteria to find compressor stage designs with high stability, and select an appropriate level of modeling in the optimization of a compressor stage using 3D CFD.

Verify the optimization methodology. This is done by re-designing all stages of a three-stage compressor using 3D CFD calculations. After the re-design, the capability of the three-stage compressor to reach the target design point at design rotational speed is evaluated. The stability of the compressor at part- and design speed needs to be considered in the design phase, and the measure used to favor high stability designs in the optimization is evaluated by replacing blade geometries to achieve higher stability at part- or design speed for the complete three-stage compressor. Furthermore, a transonic fan is optimized using the same design tool. Finally, a simulation is run of the complete low-pressure compression system of a geared turbofan engine.

Evaluate the impact of surface irregularities on performance of a transonic compressor. The impact of surface roughness on optimal blade design is evaluated. Moreover, the impact of manufacturing manufacturing variations on performance parameters and the flow field is studied by utilizing scanned geometric data of a manufactured compressor blisk.

2 Design

2.1 Requirements

A set of requirements are imposed on the design obtained from an optimization. The compressor should reach the design point, which can be specified as the total pressure ratio (P_{02}/P_{01}) across the stage and corrected mass flow rate at a given corrected rotational speed of the compressor. To obtain the corrected mass flow, the mass flow is adjusted using a reference inlet total pressure and total temperature as shown in Eq. 2.1.1, where the reference conditions is typically set as standard sea level (SLS) conditions where the total temperature $T_{0,ref}$=288.15 K and the total pressure $P_{0,ref}$=101 325 Pa.

$$\dot{m}_{corr} = \dot{m}\frac{\sqrt{T_0/T_{0,ref}}}{P_0/P_{0,ref}} \tag{2.1.1}$$

The corrected rotational speed (N_{corr}) can be specified as shown by Eq. 2.1.2.

$$N_{corr} = \frac{N}{\sqrt{T_0/T_{0,ref}}} \tag{2.1.2}$$

In the design phase, a given radial swirl angle variation at the exit from a stage may be desired and the compressor should operate safely and with high efficiency, discussed more in the following sections.

2.1.1 Surge margin

The surge margin (SM) is the distance between the operating line and the surge line in the compressor map, previously illustrated in Fig. 1.1.2, and it needs to be sufficiently large to ensure stable operation of the compressor for a range of operating conditions. The surge margin can be defined in numerous different ways, *e.g.* as shown in Eq. 2.1.3, reproduced from [9].

$$SM = \left(\frac{PR_{TT,limit} \times \dot{m}_{ref}}{PR_{TT,ref} \times \dot{m}_{limit}} - 1\right) \times 100 \tag{2.1.3}$$

Where PR_{TT} is the total pressure ratio and $\dot{m}$ is the mass flow. The subscripts *limit* and *ref* denotes an operating point at the surge line and an operating point along the operating line at the same rotational speed, respectively. The surge margin requirement is set based on experience and needs to be sufficient for the compressor to operate safely with respect to variations of the incoming flow field during flight, at different different rotational speeds, and with respect to the time it takes for the air flow through the compressor to stabilize in response to changes in the rotational speed. Furthermore, surface degradation and variations in the distance between the rotor blades and the shroud called the tip clearance or tip gap are factors that can impact the stable operating range of the compressor [10, 11].

Accurately predicting the stall process in a compressor from computational fluid dynamics (CFD) calculations is a difficult task. The process depends on the geometry of the stage (which varies with *e.g.* rotational speed and temperature), the geometry downstream of the stage and the incoming flow field which may vary in time. The stall process is a transient phenomenon, which means that a time dependent solution must be obtained if accurately resolved. It involves redistribution of the flow in the annulus, where some blade passages may be stalled while others are not [8]. Limitations in terms of mesh quality and mesh resolution, as well as the turbulence model often used in CFD calculations add many degrees of complexity to the challenge. As the level of detail included in the calculations increase, so does the required computational power which is one of the reasons why a number of simplifications are done in the initial design phase of a compressor. Furthermore, the design of adjacent components may not have been set yet, and detailed information on the incoming flow field may not be available. In the design phase, steady state calculations are often employed and the computational domain may be reduced to only include one blade passage per blade row, using a periodic boundary condition to account for the full annulus. The interface between rotating and stationary domains is typically set as a mixing plane which removes detailed wake information from one component to the next. The simplifications made, some out of necessity to be able to evaluate a large number of designs, others from the lack of detailed knowledge in the early stages of the design process make it difficult to predict the last stable operating point at the lower end of the mass flow range.

Static pressure rise capability

To be able to rank designs from low to high stability, the highest possible static pressure increase averaged for the rotor and stator, as defined in Eq. 2.1.4, is used in this thesis, which was used in [12] to evaluate the static pressure rise coefficient at stall for a large number of stages, where a correction factor for the dynamic pressure entering a blade row was also considered.

$$C_{p,rs} = \frac{(P_3 - P_2) + (P_2 - P_1)}{(P_{02} - P_2) + (P_{01,rel} - P_1)} = \frac{P_3 - P_1}{(P_{02} - P_2) + (P_{01,rel} - P_1)} \tag{2.1.4}$$

Where P is the pressure, 0 denotes total/stagnation condition and the locations 1, 2 and 3 denotes the rotor inlet, rotor outlet/stator inlet and the stator outlet, respectively. The idea is that a compressor blade row with a higher possible maximum pressure rise capability is more robust to variations of the incoming flow field. By using the measure in Eq. 2.1.4, the blade rows are compared to diffuser performance as the stages are ranked by their capability to diffuse the flow. The diffuser analogy is illustrated in Fig. 2.1.1 for subsonic flow in a compressor cascade. If the outlet flow angle from the blade row is assumed to remain constant, the outlet area A_2 illustrated in Fig. 2.1.1a also remains constant. An increase in incidence lead to a reduction of the the inlet area A_1 as illustrated in 2.1.1b, thereby increasing diffusion as the area ratio A_2/A_1 increase.

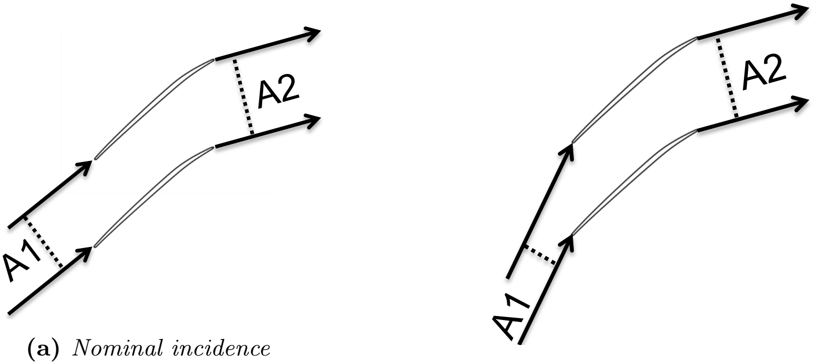

(a) *Nominal incidence*

(b) *Higher incidence*

Figure 2.1.1: *Inlet and outlet passage areas illustrated as incidence is varied.*

2.1.2 Efficiency

The efficiency of the compressor should be as high as possible. In particular, the efficiency should high at the design point. The polytropic efficiency, as defined in in Eq. 2.1.5, is here used here to quantify the efficiency of a stage.

$$\eta_p = \frac{\gamma - 1}{\gamma} \frac{\log\left(\frac{P_{02}}{P_{01}}\right)}{\log\left(\frac{T_{02}}{T_{01}}\right)} \tag{2.1.5}$$

2.2 Multi-stage considerations

When designing a blade row in an axial compressor it is important to remember that it is part of a larger component. Rather than designing a rotor in isolation, it is more appropriate to consider the rotor as part of a stage by including the downstream stator. The stator should diffuse the flow with a low level of loss. Furthermore, the stator blade row should be able to operate for a range of incidence without the flow separating. Going one step further, the stage can be considered as part of a compressor with multiple compressor stages. Depending on the rotational speed, the stable operating range for a multi-stage compressor will typically be limited by different stages, and this needs to be considered in the design phase. How the stable operating range of a multi-stage axial compressor can be limited by different stages at part- and design speed is discussed in [7], and is summarized here.

Design rotational speed

If the compressor is working at the design point and a throttle valve downstream of the compressor is gradually closed, the decrease in flow coefficient ($\phi = C_x/U$) lead to an increase in pressure ratio across the first stage which lead to an increase in density. The increase in density across the first stage result in a further reduction of the flow coefficient at the inlet to the second stage. This effect accumulates downstream in the compressor across each stage. As the throttle valve is gradually closed, typically one of the stages downstream of the first stage limit the stable operating range of the compressor as stall ensues, which may lead to surge. An increase of the flow coefficient at the inlet of the first stage will have the opposite effect, *i.e.* driving downstream stages to choke.

Part rotational speed

As the rotational speed of a compressor is reduced, the mass flow typically decrease more rapidly than the rotational speed [7]. However, since the duct area is dimensioned for the compression done at design rotational speed, the axial velocity increase further downstream in the compressor. This means that the incidence increase for the first stage relative to the design condition, while downstream stages see a decrease in incidence due to the increased axial velocity. The result is that stall typically occur in the front stage at part speed conditions for a multi-stage compressor.

The summary given here was a broad description on what can be expected at different operating conditions. However, other factors which were not discussed above can influence the stable operating range, *e.g.* distorted inlet conditions can trigger separation in the front stages at operating conditions where the rear stages were expected to limit the operating range.

3 CFD Modeling

THE present section describe different aspects of CFD modeling with respect to its implementation on the in-house CFD solver volsol++, which is the CFD solver used in Paper I, II, III, IV and V as well as for the optimization of the low-pressure compression system for a geared turbofan engine presented in *Section* 5.1.

3.1 Governing equations

The Reynolds averaged Navier-Stokes equations in conservative form for conservation of mass, momentum and energy with the k-ϵ turbulence model can be written in compact form as

$$\frac{\partial Q}{\partial t} + \frac{\partial \mathcal{F}_j}{\partial x_j} = \mathcal{H} \tag{3.1.1}$$

where the state vector Q is

$$Q = \begin{bmatrix} \bar{\rho} \\ \bar{\rho}\tilde{u}_i \\ \bar{\rho}\tilde{e}_0 \\ \bar{\rho}\tilde{k} \\ \bar{\rho}\tilde{\epsilon} \end{bmatrix} \tag{3.1.2}$$

where ¯ represent a cell average and ˜ are Favre averaged variables. The flux vector $\mathcal{F}_j$ in Eq. 3.1.1 is defined as

$$\mathcal{F}_j = \begin{bmatrix} \bar{\rho}\tilde{u}_j \\ \bar{\rho}\tilde{u}_i\tilde{u}_j + \bar{p}\delta_{ij} - \tau_{ij} \\ \bar{\rho}\tilde{e}_0\tilde{u}_j + \bar{p}\tilde{u}_j - C_p\left(\frac{\mu}{Pr} + \frac{\mu_t}{Pr_t}\right)\frac{\partial \tilde{T}}{\partial x_j} - \tilde{u}_j\tau_{ij} \\ \bar{\rho}\tilde{k}\tilde{u}_j - \left(\mu + \frac{\mu_t}{\sigma_k}\right)\frac{\partial \tilde{k}}{\partial x_j} \\ \bar{\rho}\tilde{\epsilon}\tilde{u}_j - \left(\mu + \frac{\mu_t}{\sigma_\epsilon}\right)\frac{\partial \tilde{\epsilon}}{\partial x_j} \end{bmatrix} \tag{3.1.3}$$

where the temperature ($\tilde{T}$) is Favre averaged, μ is the dynamic viscosity, μ_t is the turbulence viscosity, C_p is the specific heat at constant pressure, δ_{ij} is the Kronecker delta, Pr is the Prandtl number and Pr_t is the turbulent Prandtl number set as a 0.9. The transport equations for the turbulence dissipation and turbulence kinetic energy contain the model constants $C_{\epsilon 1}$=1.44, $C_{\epsilon 2}$=1.92, σ_ϵ=1.3 and σ_k=1.0. The source vector $\mathcal{H}$ is defined as

$$\mathcal{H} = \begin{bmatrix} 0 \\ 0 \\ 0 \\ P_k - \bar{\rho}\tilde{\epsilon} \\ \left(C_{\epsilon 1} P_k - C_{\epsilon 2}\bar{\rho}\tilde{\epsilon}\right)\frac{\tilde{\epsilon}}{\tilde{k}} \end{bmatrix} \tag{3.1.4}$$

Using the k-ϵ turbulence model with a realizability constraint, the turbulent viscosity μ_t is given as

$$\mu_t = \min\left(C_\mu \bar{\rho}\frac{\tilde{k}^2}{\tilde{\epsilon}}, \frac{0.4\bar{\rho}\tilde{k}}{\sqrt{\tilde{S}_{ij}\tilde{S}_{ij}}}\right) \tag{3.1.5}$$

where C_μ is a constant set as 0.09. The Reynolds stresses are modeled with the Boussinesq approximation, giving the viscous stress tensor (τ_{ij}) as

$$\tau_{ij} = (\mu + \mu_t)\left(2\tilde{S}_{ij} - \frac{2}{3}\frac{\partial \tilde{u}_k}{\partial x_k}\delta_{ij}\right) - \frac{2}{3}\bar{\rho}\tilde{k}\delta_{ij} \tag{3.1.6}$$

where Favre-average strain rate tensor $\tilde{S}_{ij}$ is defined as

$$\tilde{S}_{ij} = \frac{1}{2}\left(\frac{\partial \tilde{u}_i}{\partial x_j} + \frac{\partial \tilde{u}_j}{\partial x_i}\right) \tag{3.1.7}$$

the turbulence production term P_k is given by

$$P_k = \left(\mu_t\left(2\tilde{S}_{ij} - \frac{2}{3}\frac{\partial \tilde{u}_k}{\partial x_k}\delta_{ij}\right) - \frac{2}{3}\bar{\rho}\tilde{k}\delta_{ij}\right)\frac{\partial \tilde{u}_i}{\partial x_j} \tag{3.1.8}$$

For the applications considered here, the temperature vary in the range 250–400 K where the gas can be considered to be a calorically perfect gas [13]. For a calorically perfect gas, the following relationships between temperature, internal energy and enthalpy applies

$$e = C_v \tilde{T} \tag{3.1.9}$$

$$h = C_p \tilde{T} \tag{3.1.10}$$

$$C_v = C_p - R \tag{3.1.11}$$

where R is the gas constant and C_v is the specific heat at constant volume. Furthermore, the ideal gas law is used as shown by Eq. 3.1.12

$$p = \rho R T \tag{3.1.12}$$

The dynamic viscosity μ varies with temperature according Sutherlands law

$$\mu = \mu_{ref}\left(\frac{T}{T_{ref}}\right)^{3/2}\frac{T_{ref} + S}{T + S} \tag{3.1.13}$$

where μ_{ref} and T_{ref} is the dynamic viscosity and temperature at a reference condition, and S is the Sutherland constant (here set as 110 K).

3.2 Discretization

The convective flux across each cell face is calculated using a third order upwind scheme. The solution variables in primitive form are estimated at the cell face by averaging the values in the adjacent cells. The solution variables at the cell face are then used to estimate the characteristic speeds, where the characteristic speed determines the direction used in the upwind scheme to calculate the characteristic variables. The characteristic variables are then transformed back into the solution variables on primitive form. The procedure to calculate the convective fluxes in the solver is described mathematically in [14]. Where steep gradients of pressure and density are found, a controlled artificial dissipation of Jameson type is used in, see [15].

The diffusive fluxes are obtained from spatial derivatives of the solution variables in primitive form using a centered difference approach. The temporal derivative of the flow variables can be calculated once the convective and diffusive fluxes have been obtained.

$$\frac{\partial Q^n}{\partial t} = \mathcal{K}^n \tag{3.2.1}$$

The time stepping is done using a three-stage second-order Runge-Kutta method, and is done as follows

$$\begin{aligned} Q^{*} &= Q^n + \Delta t \mathcal{K}^n \\ Q^{**} &= \frac{1}{2}[Q^n + Q^{*} + \Delta t \mathcal{K}^{*}] \\ Q^{n+1} &= \frac{1}{2}[Q^n + Q^{*} + \Delta t \mathcal{K}^{**}] \end{aligned} \tag{3.2.2}$$

where the superscript n denotes the current time step, $n+1$ denotes the next time step and the superscripts $*$ and $**$ denotes sub-time steps. The time step Δt is the time step used by the solver.

3.3 Computational grid

The computational grid is made up of hexahedral elements generated using the mesh generator G3Dmesh. The method in G3Dmesh is based on transfinite interpolation, described in [16]. The boundary layers on the blade surfaces are resolved using an O-grid while the blade passage domain is constructed using H-type blocks. The tip clearance is resolved using an O-grid block and an inner H-type block. The computational grid is shown for the blade, hub and shroud surfaces for a single stage in Fig. 3.3.1. Examples of the tip clearance mesh, depending on if a wall function or a low-Reynolds model is used, are shown in Fig. 3.3.2.

3.3.1 Grid sensitivity

The sensitivity of the flow solution to the size of the computational grid is determined by evaluating the CFD solution using a range of computational grids of increasing refinement. For optimization purposes, a large number of designs needs to be evaluated, which can impose restrictions on the size of the computational grid to achieve feasible computational times. However, the numerical setup will also influence the grid refinement requirement. For example, resolving the boundary layers require a much larger number of grid points close to the walls compared to using a wall function. This was seen in Paper I, where the number of grid cells for a computational domain with resolved boundary layers was

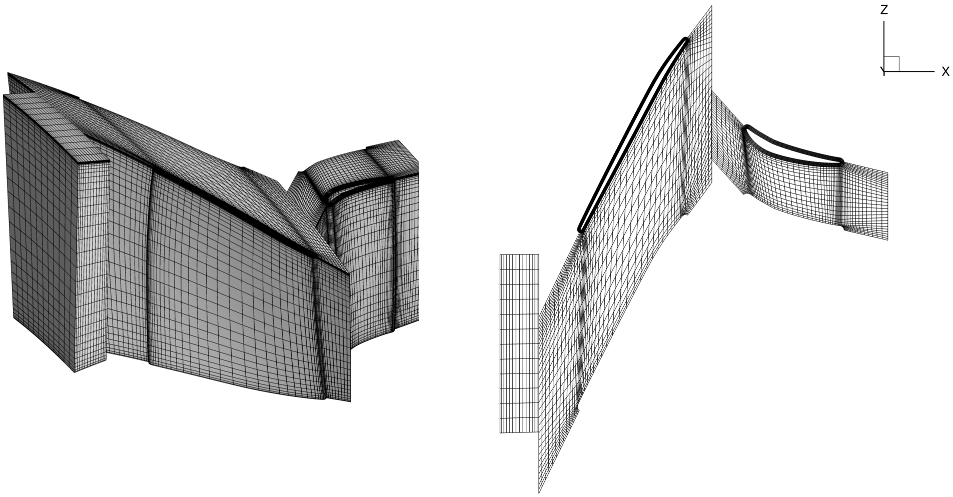

(a) *3D view*

(b) *Blade-to-blade view*

Figure 3.3.1: *Computational grid*

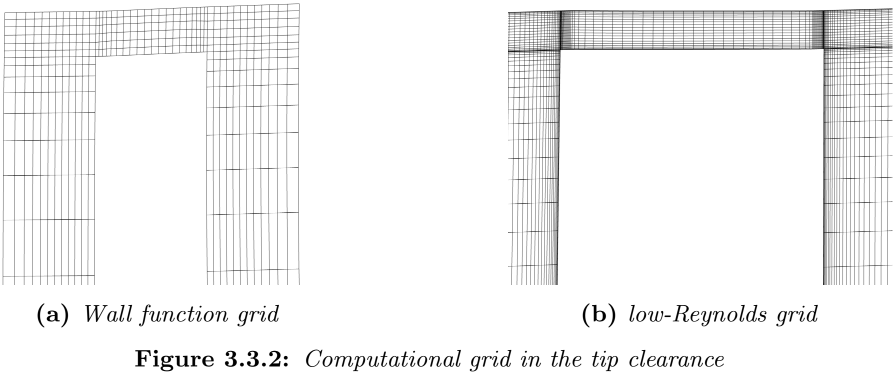

(a) *Wall function grid*

(b) *low-Reynolds grid*

Figure 3.3.2: *Computational grid in the tip clearance*

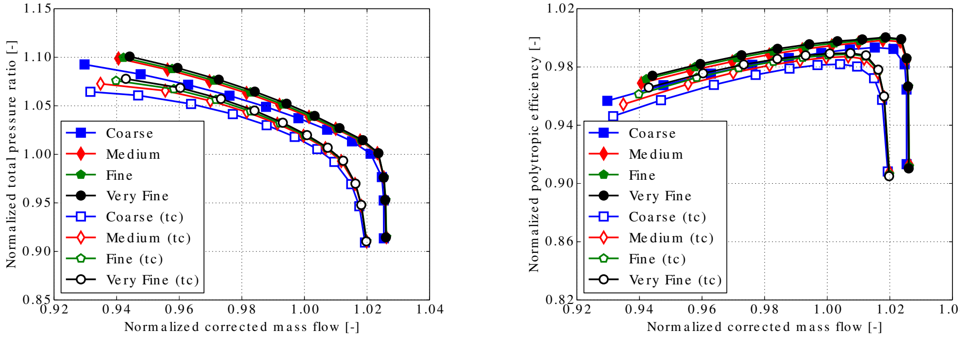

(a) *Total pressure ratio* **(b)** *Polytropic efficiency*

Figure 3.3.3: *Performance variation with grid size*

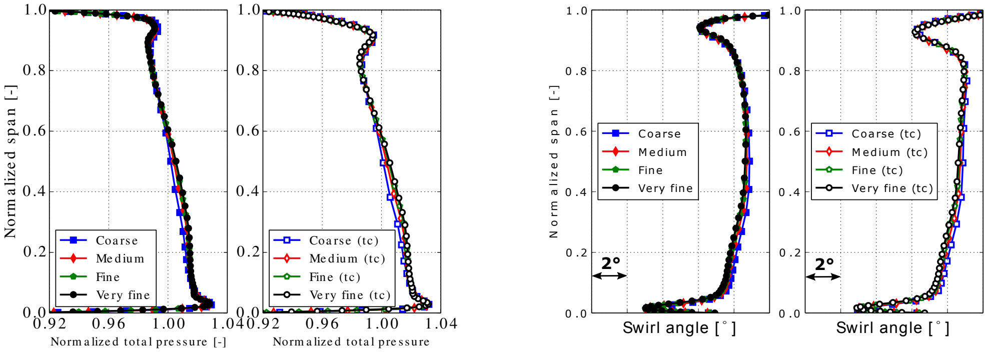

(a) *Total pressure profile* **(b)** *Swirl angle profile*

Figure 3.3.4: *Radial variation of total pressure and swirl angle with grid size*

approximately twice as large compared to a grid adapted for using a wall function to achieve the same level of sensitivity of the solution to additional refinement. Furthermore, including the tip clearance will also have an impact on the number of grid cells.

The mesh dependence of mass flow, total pressure and polytropic efficiency for the first stage compressor in the compressor re-designed in *Section* 5.1 with and without the rotor tip clearance of 0.7% normalized with the blade span are shown in Figure 3.3.3. The mesh sizes are listed in Table 3.3.1, where the configurations considering a rotor tip clearance are denoted *tc*. The radial swirl angle and total pressure distribution at the exit for the same stage resolved using the different grid sizes are shown in Fig. 3.3.4. For the studies performed as part of this work, the size of the computational grid used for optimization has typically been set to be around 100 000 grid cells in each domain, corresponding to the *Medium* grid in Table 3.3.1 (*e.g.* in Paper III, Paper IV and for the optimization of the low-pressure compression system for a geared turbofan engine presented as part of *Section* 5.1).

Table 3.3.1: Number of grid cells in the rotor/stator

Size	Coarse	Medium	Fine	Very fine
Rotor	51 000	99 000	198 000	398 000
Stator	53 000	101 000	207 000	411 000
Rotor (tc)	51 000	103 000	200 000	404 000
Stator (tc)	50 000	101 000	200 000	399 000

3.4 Boundary conditions

The simulations used for optimization are run as steady state of a single blade passage in each blade row, using a rotational periodic boundary condition to account for the full annulus. The inlet boundary condition is set as a mixed pressure boundary condition, with a radial distribution of total pressure, total temperature, the direction of the velocity vector, the turbulence kinetic energy (k) and the turbulence dissipation (ϵ). The inlet boundary condition preserves the inlet flow angle in an absolute frame of reference. Mixed implies that the inlet boundary condition switches between a fixed value or zero gradient based on the sign of the fluxes discussed in the previous section. The outlet boundary condition is set as a non-reflective (absorbing) boundary condition described in [17] based on the method of characteristics. The sides of the domains in the circumferential direction are set as rotational periodic, as shown in Fig. 3.4.1.

Mixing planes described in [18] are used at the interfaces between blade rows, where the flow is averaged circumferentially and a full conservation of the fluxes is assured by

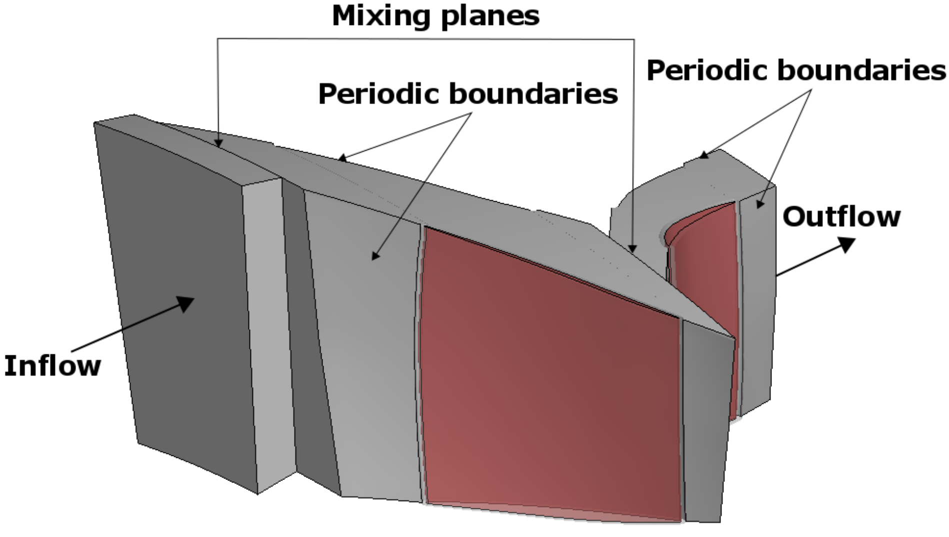

Figure 3.4.1: *Compudational domain*

correcting the flux so that the upstream and downstream side of the interface have the same average value. The mixing plane formulation is based on the method of characteristics, and has non-reflective properties. By averaging the flow in the circumferential direction, the flow is essentially mixed in this direction which results in an increase in entropy across the mixing plane. The assumption is that the same degree of mixing loss generated at the mixing plane would be generated if the flow would mix downstream in the compressor. However, the realization of losses in the mixing process across a mixing plane boundary can lead to an over-estimation of loss. Part of the energy in a wake which is realized as losses in a mixing plane may be recovered in a process called wake stretching as the wake convects downstream as described in [19]. It is discussed in [20] that since most of the mixing of a wake from an airfoil takes place within the distance of a few trailing edge thicknesses, discrepancies between a simulation utilizing a mixing plane compared to an results where mixing is not enforced at the interface, would mainly be associated with large three-dimensional features near the end-walls.

3.4.1 Wall modeling

The walls are specified as adiabatic no-slip walls, *i.e.* there is no heat transfer through the walls and the velocity directly adjacent to the surface is zero. A non-dimensional distance from a wall can be calculated as

$$y^+ = \frac{u_* y}{\nu} \tag{3.4.1}$$

where y is the distance from the wall, ν is the kinematic viscosity and u_* is the friction velocity defined in Eq. 3.4.2.

$$u_* = \sqrt{\frac{\tau_w}{\rho}} \tag{3.4.2}$$

Where ρ is the density and τ_w is the wall shear stress. For turbulent flow near a wall, the flow can be divided into three regions: the viscous sublayer closest to the wall where viscous shear dominate, an overlap layer where both viscous and turbulent shear are important, and an outer layer where turbulent shear dominates. Closest to the wall ($y^+ < 5$), in the viscous sublayer, it is found the linear relation in Eq. 3.4.3 well describes the velocity variation.

$$u^+ = y^+ \tag{3.4.3}$$

where u^+ is the non-dimensional velocity defined as shown by Eq. 3.4.4.

$$u^+ = \frac{u}{u_*} \tag{3.4.4}$$

In the overlap layer it is found that the velocity variation can be expressed logarithmically as

$$u^+ = \frac{1}{\kappa} \ln(y^+) + B \tag{3.4.5}$$

where κ is the von Karman constant (≈ 0.41), ln is the natural logarithm and B is a constant (≈ 5.0). When a wall function is used, the first grid point away from the wall is placed in the overlap layer and the logarithmic relation shown in Eq. 3.4.5 is used. For low-Reynolds models, the boundary layer profile is resolved by placing the first grid point away from the wall in the viscous sublayer.

3.5 Geometric representation

3.5.1 Tip clearance

An axial compressor consists of rotating and stationary blade rows, where the distance between the rotating blades and the inner casing (shroud) is called the tip clearance or tip gap, and is required to avoid contact of the blades with the shroud during engine operation. The tip clearance is a geometric feature of high importance as it can have a significant impact on the surge margin and efficiency of the compressor. Thermal expansion of the casing and elongation of blades due to centrifugal forces are factors that need to be taken into account when specifying the tip clearance size in the design phase. Furthermore, g-forces *e.g.* during landing can momentarily alter the tip clearance in an aircraft engine.

Although the radial size of the tip clearance could be considered small, usually in the order of millimeters or part of a millimeter, it can have a large impact on performance. Depending on the size of tip clearance relative to the size of the compressor blade, its influence on performance can range from negligible to substantial where it has a considerable adverse impact on efficiency and on the stable operating range of the compressor. In [21] it was shown that for a tip clearance size below 0.4% of the blade span, the impact on efficiency was small. This was also shown in [22] and [23] where the performance for a small tip clearance (approximately 0.4% span) showed close agreement with simulation results obtained using a computational model without tip clearance. For a larger tip clearance, the tip clearance flow can have a significant adverse impact on performance. This was illustrated in [23] where the polytropic efficiency decreased by more than 3% in both the computational investigation and the experiment when a tip clearance size was increased from approximately 0.4% to 1.2% of the blade span.

Tip clearance flow, illustrated in Fig. 3.5.1, is mainly driven by the pressure difference between the pressure and suction sides of the blade at the tip [24]. Separation and re-attachment of the flow can occur in the tip clearance [25]. Part of the flow that passes through the clearance rolls up to a vortex, called a tip clearance vortex illustrated in Fig. 3.5.1. For small tip clearances, the main contribution to losses associated with the tip clearance is caused by viscous shear loss generated at the shroud [21]. As the clearance increases in size, losses due to mixing of the tip clearance flow become dominant. In [21] it was shown that an optimal tip clearance size with respect to losses can exist which is explained in terms of the competing loss mechanisms: viscous shear loss at the shroud and tip leakage mixing loss. There is a tip clearance size for which the sum of these two loss sources is at a minimum, which was in the range 0.1-1% of the blade span for the compressors analyzed in [21].

Impact on surge margin

An increase in tip clearance size can significantly reduce the surge margin of a compressor stage [11]. The topic of stall associated with tip clearance flow is discussed in numerous publications, *e.g.* for a subsonic compressor in [26] and for a transonic compressor in [27]. In [27], the onset of stall in a transonic compressor was studied using Large Eddy Simulations (LES) and by comparing the computational results with experimental measurements. The stall process for the investigated compressor is well described in the study and will here be summarized. Random oscillation of the tip clearance vortex and its interaction with the passage shock is described to be the main trigger for the occurrence of a rotating stall cell. The onset of a rotating stall cell is explained by the formation of a stall cell downstream of the sonic plane in the tip region, where the region of low momentum flow influence the adjacent blade passage. The route from a near stall operating condition to the formation of a rotating stall cell is described below.

- The passage shock fully detaches.
- A low momentum area is formed near the pressure side of the compressor blade, triggered by interaction of the tip clearance vortex and the passage shock.
- As the mass flow decrease, the low momentum area moves upstream and reversal of the tip clearance flow occurs at the trailing edge, impinging on the pressure side of the adjacent rotor blade.
- Low momentum flow, as well as an induced vortex (originating from tip clearance flow from 20-60% chord), reach the leading edge and tip clearance flow spill over the leading edge of the adjacent blade.

Since the passage shock is fully detached, the events described above occur downstream of the sonic line and the stalled region can move circumferentially as a rotating stall cell. The impact of tip clearance flow on the flow in the passage is not limited to the tip region, but can affect the flow far away from the tip region as shown in [28]. Due to a larger region of low momentum fluid in the tip region of a rotor as the tip clearance size was

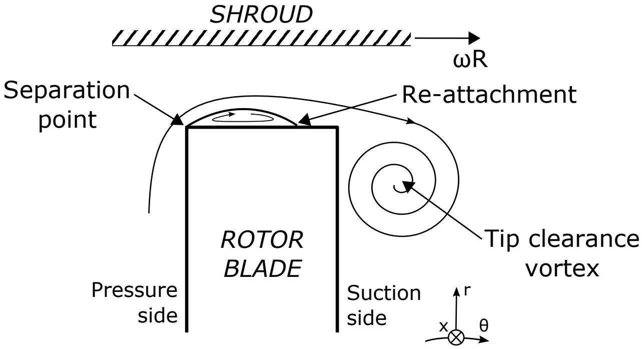

Figure 3.5.1: *Tip clearance flow illustration in a relative frame of reference*

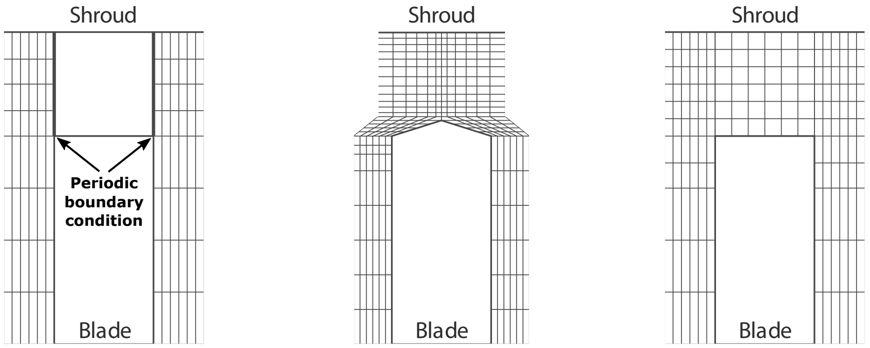

(a) *Periodic boundary* **(b)** *Pinch-tip model* **(c)** *Multi-block approach*

Figure 3.5.2: *Tip clearance modeling approaches*

increased in [28], the overall passage diffusion decreased which reduced a local separation at the hub. In Paper II of this thesis it was shown that including the tip clearance in the design phase can impact an optimal blade design across the entire blade span.

It was reported in [29] that in terms of the flow coefficient at stall, an optimum tip clearance can exist, which was reported to be 0.5% of the chord for the compressor rotor evaluated in [29]. For a smaller tip clearance, a casing corner separation caused a leading edge separation in the tip region, while for a 0.5% tip clearance or larger, spillage of the tip leakage jet caused the leading edge separation. Furthermore, it was concluded in [29] that shifting the distribution of axial momentum through the tip clearance towards the trailing edge increased the flow range for a geometry where the flow range was limited by the leakage jet, while an aft shift of the axial momentum reduced the flow range for a geometry limited by a casing corner separation.

Tip clearance modeling

The tip clearance of a compressor rotor is typically modeled in one of three ways. The tip clearance can be set as a periodic boundary, it can be gridded using a ”pinch-tip” approach, or it can be gridded using a multi-block approach. By applying a periodic boundary condition over the blade tip, see Fig. 3.5.2a, the tip clearance is not resolved but still allows for a mass flow through the clearance. This approach has been used in multiple studies, *e.g.* in [30–32]. By setting a periodic boundary condition, viscous losses and mixing effects over the blade tip are neglected. Flow separation in the tip clearance, which in reality would cause blockage of the flow, can be accounted for by changing the radial size of the tip clearance used in the computational model. The relation between the size of the modeled tip clearance and the true geometrical tip clearance must therefore be evaluated on a case-to-case basis.

The pinch-tip approach, illustrated in Fig. 3.5.2b, was used *e.g.* in [32–35] and require a zero blade thickness at the tip. In order to achieve this, the blade tip corners can be rounded or the tip geometry can be changed to a wedge shape to extend the computational grid into the tip clearance. This is done to avoid adding complexity, but often at the expense of quality, to the computational grid. Similar issues as for the periodic boundary can be seen [20]. The multi-block approach, illustrated in Fig. 3.5.2c, where the tip clearance is fully resolved with a separate grid block has become more common as the level of fidelity of simulations has increased. The multi-block approach was used *e.g.* in [36–38] and is attractive since it does not require any modification of the blade geometry.

The three approaches described above to model tip clearance were compared for a low-speed compressor in [25]. The tip clearance size was reduced in size when the pinch-tip and periodic boundary condition interface were used since flow separation was suspected to occur along the blade tip. The pinch-tip model over-predicted the total losses, while using the periodic boundary condition in the tip clearance resulted in an under-prediction. The best overall agreement with experimental data was obtained using the multi-block approach. A systematic comparison of different tip clearance modeling approaches was also made in [39], where it was concluded that a fully resolved tip clearance using a multi-block approach showed best agreement with experimental data.

The multi-block approach is the method used to resolve the tip clearance in this thesis for all studies where the tip clearance was considered (Papers I, II, V and in the optimization of the low-pressure compression system for a geared turbofan engine presented described in *Section* 5).

3.5.2 Surface roughness

An increase in surface roughness on compressor blades is known to have an adverse impact on performance [10, 40, 41] and, consequently, increase the fuel consumption of a turbomachine. The impact of surface roughness depends on the Reynolds number, and for low Reynolds numbers surface roughness could have a positive impact by reducing or even avoiding flow separation by triggering earlier transition from laminar to turbulent flow. Transition from laminar to turbulent is also influenced by the turbulence level, which is relatively large in compressors [8], so that the boundary layers are typically assumed to be fully turbulent. The Reynolds number is typically high in an axial compressor, *e.g.* it was reported to be around $1.5{\cdot}10^6$ based on the rotor chord at design rotational speed for the transonic compressor investigated in Paper I, and around $1 \cdot 10^6$ for the compressors investigated in Paper III and Paper V. At high Reynolds numbers, surface roughness mainly impact the flow by causing a thicker boundary layer. In the design phase, the surface of a compressor blade is typically assumed to be hydraulically smooth which can be a good assumption for a newly manufactured blade. However, once the aircraft engine is in service, surface degradation ensues as the engine is exposed to a wide range of environmental conditions where particles of varying sizes and compositions enter the air intake. Surface roughness is most commonly measured and reported as R_a [42], which is the arithmetic average of the distance (y_i) from the mean line for a number of measurements as defined in Eq. 3.5.1.

$$R_a = \frac{1}{n}\sum_{i=1}^{n}|y_i| \tag{3.5.1}$$

Note that R_a does not distinguish between peaks or valleys. Another common measure is the root mean square deviation of the measured profile from the mean line, R_q, defined in Eq. 3.5.2. The two measures, R_a and R_q, as well as the mean line are illustrated for an artificial surface profile in Fig. 3.5.3.

$$R_q = \sqrt{\frac{1}{n}\sum_{i=1}^{n}y_i^2} \tag{3.5.2}$$

Experimental measurements of flow in rough pipes were presented in 1933 in [43], a report which was later translated into English in 1950 in [44]. In the study, sand grains were applied to the inside of pipes to study the effect of surface roughness on the wall boundary layer and the results are still in use today as part of numerical models. To model the effect of surface roughness, the measured surface roughness is thus often converted to an equivalent sand grain roughness, k_s. Different conversion factors, ϵ, are used to obtain an estimated sand grain roughness depending on the format used to describe the measured level of surface roughness. The value of the conversion factor vary in literature, and a range of conversion factors for R_a and R_q reported in [45] for surfaces used in gas turbines from a large number of publications are shown in Table 3.5.1. The table show that the conversion factor reported for surfaces in gas turbines vary considerably.

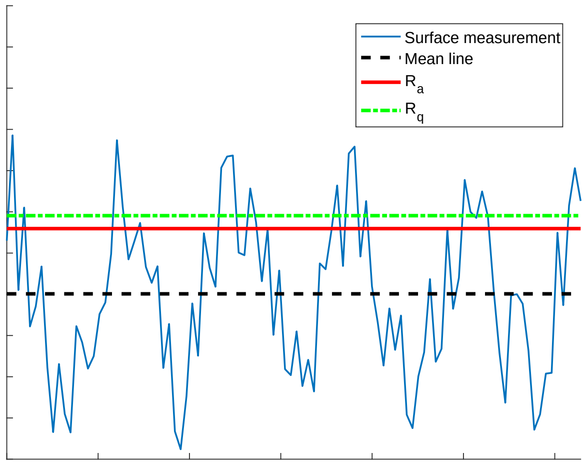

Figure 3.5.3: *Surface roughness profile*

Table 3.5.1: Surface roughness conversion factors from [45]

Roughness parameter	Estimated sand grain roughness conversion factor (ϵ)
R_a	1.8–10
R_q	2.1–4.8

The conversion factor was studied in [46], where it was shown that converting R_a to an equivalent sand grain roughness size using a single value of the conversion factor is too much of a simplification. In the study, it was shown that the relation between R_a and k_s depends on the roughness topology, which was described by a roughness slope determined by normalizing the roughness amplitude with the distance between roughness peaks. Depending on the roughness slope, the conversion factor for R_a in [46] varied in the range 2.5–9.

CFD Model

The surface roughness model in ANSYS Fluent [47] was implemented in the in-house CFD solver volsol++ and used in Paper III where the impact of surface roughness was accounted for by applying a shift ΔB to the law of the wall as shown in Eq. 3.5.3.

$$u^+ = \frac{1}{\kappa}\ln(y^+) + B - \Delta B \tag{3.5.3}$$

The shift of the law of the wall, ΔB, depends on the value of an equivalent sand grain roughness Renyolds number k_s^+ defined in Eq 3.5.4.

$$k_s^+ = \frac{u_* k_s}{\nu} \tag{3.5.4}$$

The shift of the log law when surface roughness is considered is illustrated in Fig. 3.5.4. The surface roughness model in ANSYS Fluent accounts for three regions, a hydraulically smooth regime ($k_s^+ <= 2.25$), a transitional regime ($2.25 < k_s^+ <= 90$) and a fully rough regime ($k_s^+ > 90$). Formulas for ΔB proposed in [48], based on data presented for pipes coated with sand grains in [43], are used for the different regimes. For the hydraulically smooth regime there is no shift of the log law. More information on the model and its implementation can be found in [47].

Impact on performance

It was reported in [10] that R_a is in the range 1.53–2.03 μm for stator blades in a modern turbofan engine after a long period of in-service use, and in [40] it was reported that a rough coating with R_q in the range 2.54–3.18 μm was representative of the in-service roughness levels of a fan blade. In [40], the adiabatic efficiency decrease which could be attributed to an increase in surface roughness was in the range 1–3% at design rotational speed. The impact of surface roughness on performance of a transonic compressor stage was investigated in Paper III of this thesis. In Paper III, a reduction of the polytropic efficiency by 3.5–3.8% was seen for a number of designs at the design point when an

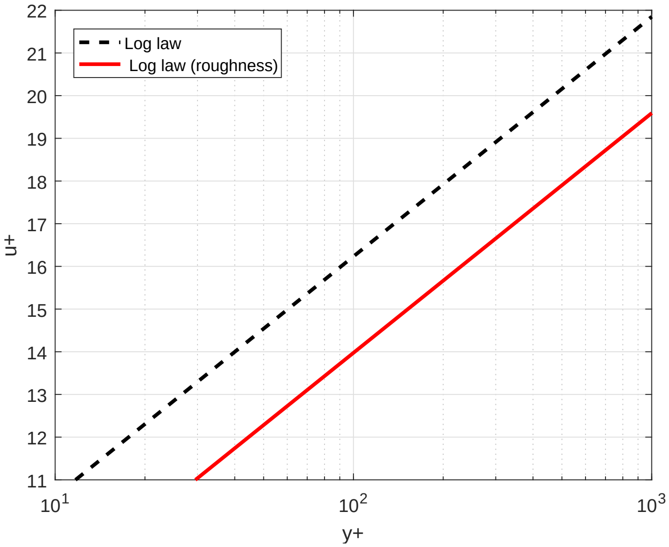

Figure 3.5.4: *Law of the law. With and without considering surface roughness.*

equivalent sand grain roughness of 16 μm was specified on the blade surfaces. Using the conversion factor found in [49], which correspond to a roughness slope of around 13% [46], gives that k_s of 16 μm corresponds to an R_a of approximately 2.6 μm. However, considering the range of conversion factors reported for R_a in [46], an equivalent sand grain roughness of 16 μm could correspond to R_a in the range 1.8–6.4 μm depending on the roughness slope.

In paper III, it was concluded that compressor blades could be designed without accounting for surface roughness. This was determined by comparing the performance for blades optimized considering smooth surfaces, which were subsequently degraded, to the performance of blades optimized taking surface roughness into account. The difference in performance was shown to be small. In a previous study [10] using a similar model to account for surface roughness, it was found that a region of separated flow increased in size as surface roughness was increased. On this basis, it is recommended to design blades considering smooth blade surfaces, and to subsequently evaluate the performance of selected designs considering surface roughness.

The study presented in Paper III was made with a restriction of the design variables of ±3 degrees, and to evaluate the impact of this restriction on the results, the limitation of the variable space was removed and the optimization was continued. The old and new Pareto fronts are shown in Fig 3.5.5a and 3.5.5b respectively. Three designs were selected from the new Pareto front (from the optimization considering smooth blade surface), and degraded by specifying surface roughness on the blade surfaces. For the designs optimized considering smooth blade surfaces, the rotational speed was increased by approximately

2% to reach the design point when surface roughness was considered. It is shown that the conclusion remain the same as that reported in Paper III, the degraded compressor blades that were optimized considering smooth blade surfaces are essentially part of the Pareto front from the optimization considering rough blade surfaces.

In Paper III it was noted that a separation at the stator hub limited the stable operating range for all compressor stages. It can therefore be of interest to analyze how the stator design was changed for the designs with higher stability. The main design change was found to be a reduction of the leading edge blade angle near the hub for the stator, which in turn lowered the incidence near the hub. The stator leading edge blade angle and the incidence for an operating point away from stall at 58% of the design rotational speed are shown in Fig. 3.5.6a and Fig. 3.5.6b, respectively. The reduced incidence near the hub for the highest stability design was beneficial to delay the separation.

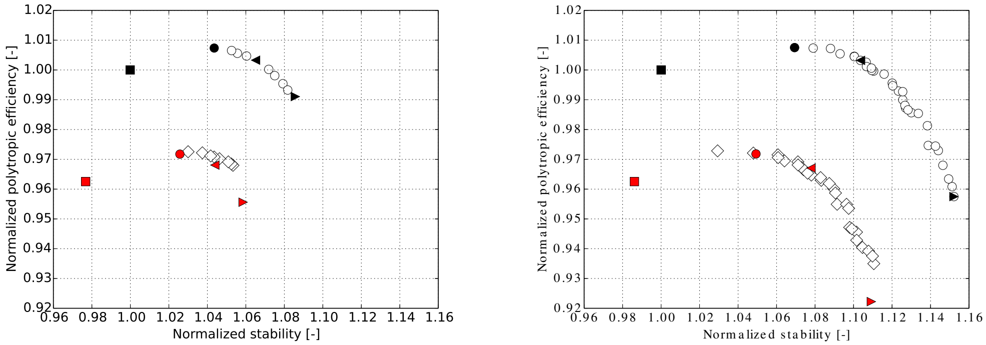

(a) *Pareto front from Paper III* **(b)** *Pareto front. Extended variable range*

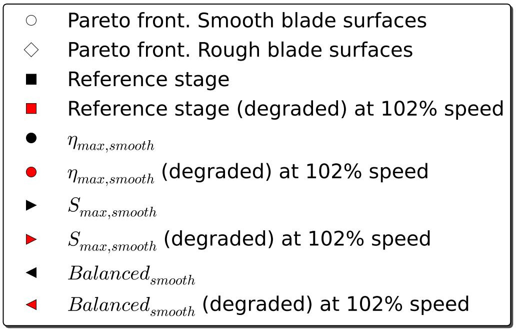

(c) *Legend*

Figure 3.5.5: *Pareto fronts from optimizations with and without surface roughness*

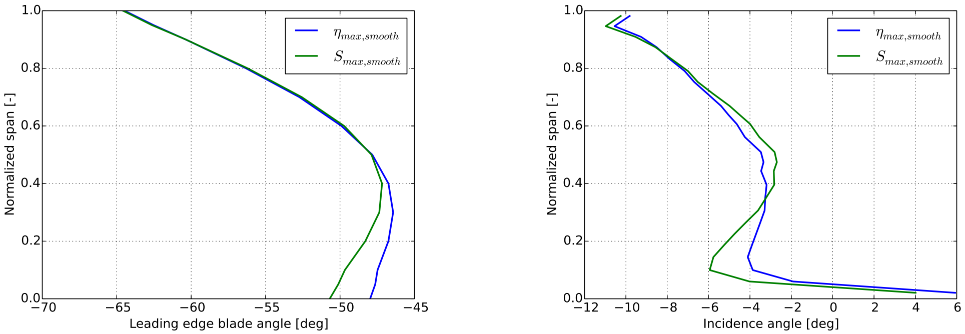

(a) *Stator leading edge blade angle* **(b)** *Stator incidence*

Figure 3.5.6: *Leading edge blade angle and incidence of optimized stator blades*

3.5.3 Manufacturing variations

The geometry of a manufactured compressor blade will deviate in some degree to the design intent due to the manufacturing process, and variations induced by the manufacturing process will typically have a detrimental impact on the aerodynamic performance as reported in *e.g.* [50–52]. In order to ensure that the manufactured product meets imposed requirements, a tolerance band is defined to determine whether a manufactured blade is acceptable, if it needs to be re-worked, or in worst case, scrapped. From a cost perspective it is thus necessary to find a sound tolerance level that balances the product performance and manufacturing cost. Ideally, a blade with large geometric deviations from the design intent would only be re-worked or scrapped if the adverse impact of this blade on the flow can be verified to be outside of the requirement specifications.

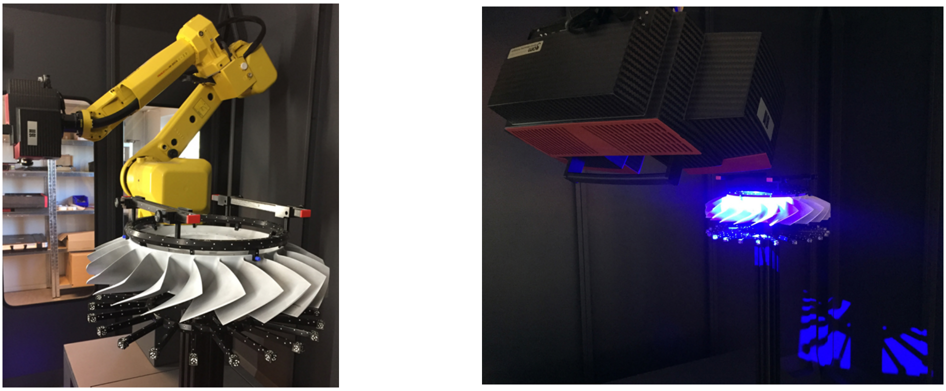

(a) *Robotic arm and optical measurement device* **(b)** *Optical measurement device in-use*

Figure 3.5.7: *Optical measurement device used for 3D coordinate measurements attached to a robotic arm*

A methodology was developed and presented in Paper VII to study the impact of manufacturing variations on aerodynamic performance. The study was made using geometric data of a manufactured bladed disk (blisk), obtained from optical measurements using the device shown in Fig. 3.5.7. The measured geometry was compared to the design intent and the geometric deviation from the design intent could be quantified for a large number of points on the blisk. The measured variations from the design intent was subsequently used to alter the computational grid of the hot blade geometry (the geometry of the blade when it is rotating at design rotational speed) with the assumption that the geometric change of the rotor blade from non-rotating to rotating has not been affected by the manufacturing variations. Figures 3.5.8 and 3.5.9 shows the mesh at the leading- and trailing edge in the tip region before and after it was deformed according to a measured geometric deviation from the design intent. The deformation takes place inside the O-grid around the rotor, with the first node on the blade surface being moved the same distance as the blade deformation, and with the mesh displacement decreasing linearly out to zero displacement at the last node of the O-grid. This ensures that 1:1 grid matching is still achieved for the outer layer of the O-grid and the connected H-grid with the grid of the next rotor blade passage when multiple blade passages are considered.

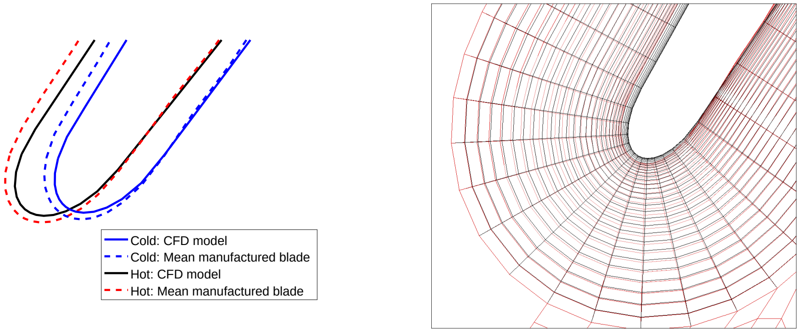

(a) *CFD model and mean manufactured geometry*

(b) *Baseline mesh (black) and manufactured blade mesh (red lines)*

Figure 3.5.8: *Geometry and mesh at the leading edge in the tip region for the CFD model and the mean manufactured geometry*

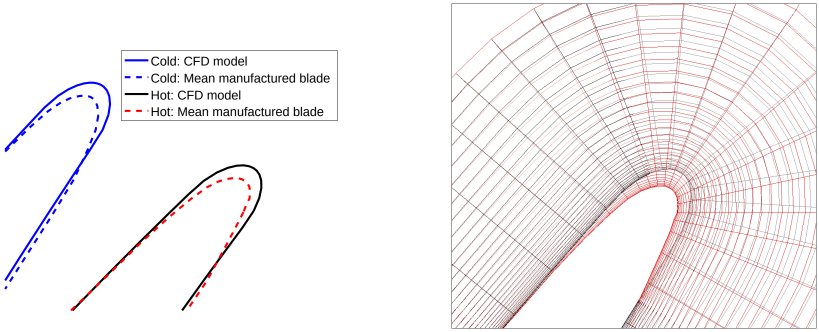

(a) *CFD model and mean manufactured geometry*

(b) *Baseline mesh (black) and manufactured blade mesh (red lines)*

Figure 3.5.9: *Geometry and mesh at the trailing edge in the tip region for the CFD model and the mean manufactured geometry*

3.6 Turbulence model

In Paper I, performance parameters and radial variations of total pressure were compared with experimental data for the k-ϵ turbulence model with wall functions and using Chien's low-Reynolds model [53] to resolve the boundary layers. As part of the grid dependence study carried out in Paper I, the influence of grid resolution in the passage and in the tip region was systematically analyzed by successive refinement of the grid in axial, tangential and radial directions. Using the low-Reynolds model, a close agreement was found for the polytropic efficiency with experimental data. Although using wall functions resulted in an under-prediction of the polytropic efficiency, the efficiency variation along the speedline was close to the experiment. The result suggest that the variation of the dominating loss mechanisms as the compressor is throttled can be captured using the k-ϵ and both wall modeling approaches. Surge margins for the results obtained using both wall modeling approaches in Paper I were calculated and presented in Paper VI, where it was determined that the surge margin (see definition in Eq. 2.1.3) was under-predicted relative to the experiment by 5% and 6.5%, using wall functions and the low-Reynolds model, respectively.

The capability of turbulence models to represent the flow field in an axial compressor rotor was investigated in [54], where it was shown that the k-ω SST model [55] was one of the turbulence models that showed best agreement with measurements in terms of the tip clearance vortex trajectory for a near stall condition. The best agreement at both the design condition and near-stall in terms of the strength of the tip clearance vortex was found using the Reynolds Stress Model [56], while a corner separation near stall was best predicted using the standard k-ϵ turbulence model [57].

Performance predictions in [23] were made using different turbulence models and computational grids for a transonic axial compressor rotor with a relatively small tip clearance of 0.65% of the tip chord (approximately 0.4% of the blade span) at part- and design speed. Two different steady state calculation setups were compared: a configuration referred to as the *design model* using the k-ϵ turbulence model and wall functions, and a model referred to as the *low-Reynolds model* where the k-ω SST model was used with a finer computational grid to resolve the boundary layers. While both models predicted similar overall performance and flow distributions, the low-Reynolds model showed a better agreement with experimental data at a part speed while the design model showed a better agreement with experimental data design speed.

From the literature reviews presented here and in Paper VI, it is concluded that using wall functions can be adequate to capture the main flow features in a compressor, and can therefore be suitable to use in an optimization. The turbulence model mainly used in this thesis (Paper I, II, III, IV, V and in the optimization of the low-pressure compression system for a geared turbofan engine presented in *Section* 5.1) is the realizable k-ϵ model with wall functions and the Kato-Launder limiter. The turbulence model was chosen a compromise between numerical accuracy and computational time.

4 Optimization procedure

4.1 Optimization algorithm

The genetic algorithm NSGA-II [58] used in this work mimics evolution in nature, representing the variable values by what is referred to as a chromosome. The algorithm works generation by generation, improving designs by crossover based on tournament selection and randomly changing chromosomes in a process referred to as mutation. Elitism is used, which means that the best individuals of each generation are allowed to remain as part of the population in the next generation. The chromosomes are mutated which helps the algorithm explore the design space and to escape from local optima, thereby increasing the chances of finding the global optima. In the tournament selection, the fitness value of two individuals is compared and given a certain probability, the winner or loser will have a chance to pass on part of its chromosome to a new individual.

For a multi-objective optimization, the designs are split into different ranks to determine the fitness value. This split is illustrated in Fig. 4.1.1 for two objective functions that should be maximized. In the figure, rank 1 designs consist of all designs that are not dominated by any other, *i.e.* no better designs exist with a higher value of both objective functions. All rank 1 designs can be considered to be non-dominated individuals and make up the Pareto front for the dataset. Another selection can be made of individuals that are only dominated by rank 1 designs, these will be designs of rank 2. This process can be repeated until all designs have been assigned a rank. This ranking is used as the fitness value in the multi-objective optimization.

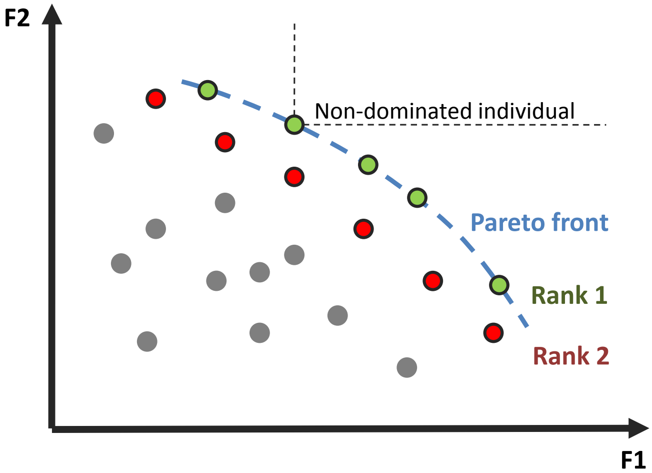

Figure 4.1.1: *Pareto front illustration*

4.2 Optimization framework

The optimization framework used in this thesis was originally developed as part of the work presented in [59], and has been further developed within the scope of this thesis. At the outset of the optimization, a latin hypercube sampling is made of the design space and the designs are evaluated using 3D CFD. The results from the CFD calculations are used to construct a response surface of each objective function and of each function that represent a constraint used to determine if a design is acceptable. In this work, a radial basis function (RBF) has been used, which was determined to be an appropriate meta model for optimization of compressor blades in [60].

When a meta model has been constructed, the optimization is done on the meta model rather than evaluating every design using CFD. An example of an RBF, constructed from the known values of an objective function *f(x)* at five data points, is shown in Fig. 4.2.1a. As shown in the figure, the RBF is equal to the known values of *f(x)* at the locations of the data points. If the function *f(x)* should be maximized, then two regions: x≈1.5 and x≈4.5, can visually be identified to be of interest. By evaluating the exact value of the function *f(x)* in these two regions, a more accurate response surface can be constructed as illustrated in Fig. 4.2.1b. This process can be repeated until no higher values of *f(x)* are found.

Rather than visually identifying regions of interest as in the example above, the optimium in the design of compressor blades in this thesis is found by using the genetic algorithm NSGA-II [58]. After optimizing on the response surface, a selection of 10 designs is made along the Pareto front which are evaluated using 3D CFD. The results from the CFD evaluation are subsequently used to update the response surface. The optimization process is illustrated in Fig. 4.2.2, where the *Design loop* is repeated until the Pareto front is converged. The optimization framework in [59], Paper II and III, utilized the commercial software ModeFRONTIER™ for optimization purposes. For the optimizations done in Paper IV and of the low-pressure compression system in *Section* 5, a genetic

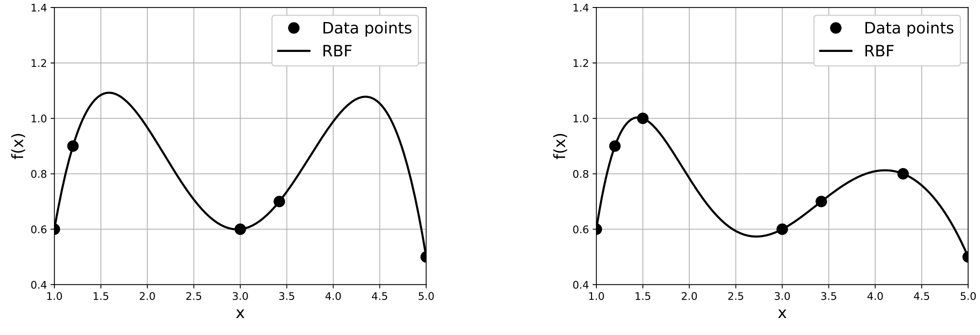

(a) *Data points and RBF* **(b)** *Updated set of data points and RBF*

Figure 4.2.1: *Inlet and outlet passage areas illustrated as incidence is varied.*

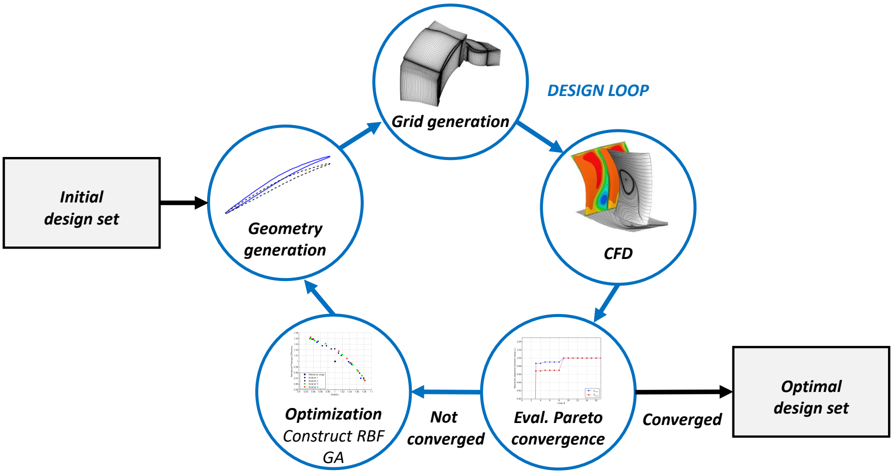

Figure 4.2.2: *Simplified overview of the optimization set-up*

algorithm coded in Python [61] was used instead. The python based genetic algorithm was integrated as part of the design loop and the design loop illustrated in 4.2.2 was to a large extent automated.

The optimization framework has successfully been used for finding high performance blade designs in Paper II, III, IV and for the design of the low-pressure compression system described in *Section* 5. The number of design loops needed to obtain a converged Pareto front depend on a number of factors, such as the number of designs used for the latin hypercube sampling and the initial variable range. If the initial variable range in the latin hypercube sampling is set too narrow, Pareto designs may be found at the limit of the allowed variable range and the range must be increased to explore a new region of the design space. Increasing the variable range can be time consuming, as a large number of designs must be evaluated to obtain a response surface representative of this new region of the design space. On the other hand, if the variable range used for the latin hypercube sampling is set too wide, difficulties can arise in terms of mesh quality, and convergence issues can arise for poor designs. The number of designs used for the initial latin hypercube sampling determine the accuracy of the first RBF. Increasing the number of initial samples will increase the computational resources required prior to constructing the first RBF, however, the investment could reduce the number of design loops needed to find a converged Pareto front. In this thesis, the number of samples used in the initial latin hypercube sampling is typically set as the number of data points required to determine the coefficients for a quadratic response surface, calculated as $(n+2)(n+1)/2$ where n is here the number of design variables [62].

The convergence of the Pareto front is evaluated by monitoring the maximum value at each end of the Pareto front as the number of design loops increase, illustrated in Fig 4.2.3a. Furthermore, Pareto designs can be plotted to show how the Pareto front is

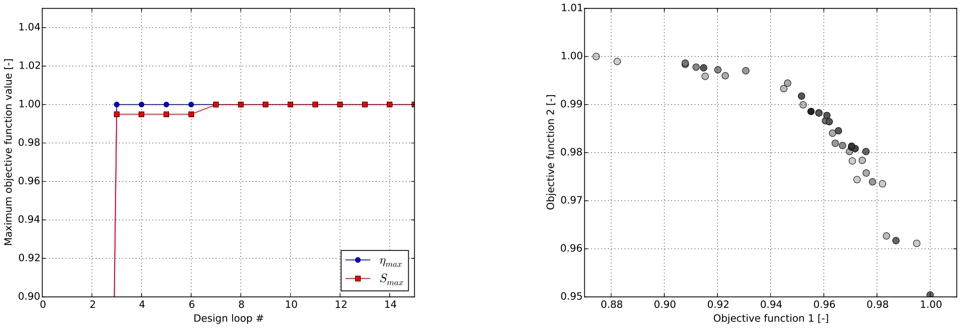

(a) *Maximum values in the Pareto front* **(b)** *Variation of Pareto front with desing loop*

Figure 4.2.3: *Pareto front evaluation*

updated as the optimization progress. This is illustrated in Fig. 4.2.3b, where designs which change the shape of a Pareto front during an optimization are shown. The marker color change from light to darker shades of grey depending on the design loop number.

4.3 Meta model

The meta model used in the present work is a radial basis function (RBF), shown to be an appropriate choice to use in optimization of compressor blades in [60]. The function value $\hat{f}$ in Eq. 4.3.1 is calculated for a point x in space as a function of the Euclidean distance r, shown as Eq. 4.3.2, to N number of neighboring known data points. To calculate $\hat{f}$, a radial basis function ϕ must be selected and a coefficient vector c_j needs to be calculated.

$$\hat{f}(x) = \sum_{j=1}^{N} c_j \phi(r) \tag{4.3.1}$$

$$r = \|x - x_j\| \tag{4.3.2}$$

The radial basis function used in this thesis is a multiquadric function as shown by Eq. 4.3.3 where ϵ is a constant.

$$\phi(r) = \sqrt{\left(\frac{r}{\epsilon}\right)^2 + 1} \tag{4.3.3}$$

In the present work, the value of ϵ was determined by removing a number of points from the data set and constructing radial basis functions using the remaining data points for different values of ϵ. The value of ϵ which returned the best approximation of the true function values of the removed data points was used to build the final radial basis function used in the design loop. Fig. 4.3.1 illustrates the change in shape of a radial basis function for different values of ϵ.

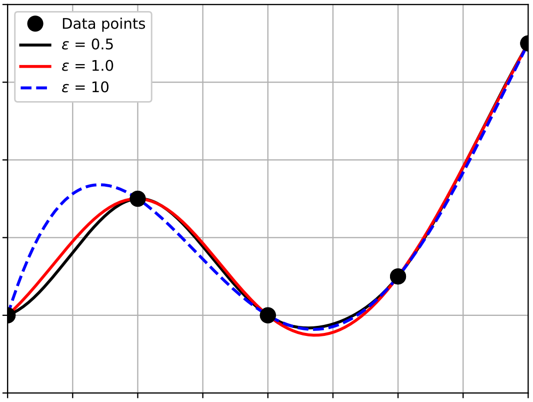

Figure 4.3.1: *Radial basis functions using different values of* ϵ

The model should return the true function values f_j at the locations of the known data points x_j. Using this criteria, the coefficients in c_j can be determined. The system of equations that needs to be satisfied is shown as Eq. 4.3.4

$$\mathbf{A} \cdot \mathbf{c} = \mathbf{f} \tag{4.3.4}$$

where the matrix $\mathbf{A}$ is calculated based on information at the known data points as shown in Eq. 4.3.5.

$$\mathbf{A} = ((\|x_i - x_j\|)/\epsilon)^2 + 1)^{1/2}, \quad i, j = 1 \in [1, N] \tag{4.3.5}$$

Since the matrix $\mathbf{A}$ is non-singular, the vector $\mathbf{c}$ can be calculated by inverting $\mathbf{A}$ as shown in Eq. 4.3.6.

$$\mathbf{c} = \mathbf{A}^{-1} \cdot \mathbf{f} \tag{4.3.6}$$

4.4 Lipschitz sampling

To reduce the risk of missing a global optima when emplying meta model assisted optimization, the meta model is updated by utilizing Lipschitz sampling [63] to additionally explore the design space in regions where the accuracy of the meta model may be low. This is done by generating a set of artificial designs by latin hypercube sampling, and a merit value is subsequently calculated for each design as shown by Eq. 4.4.1.

$$Merit(x) = L(x) \cdot Radius(x) \tag{4.4.1}$$

where $Radius(x)$ is the distance of the artificial design to the closest point of the known data set (the known data set consists of designs which have been evaluated using CFD) and $L(x)$ is the Lipschitz constant estimated as

$$L(x) = \frac{|f(x_1) - f(x_2)|}{|x_1 - x_2|} \tag{4.4.2}$$

where the indices 1 and 2 reflect data points in adjacent Voronoi cells and f is the function value at the specified data point (here the polytropic efficiency or the stability measure). Voronoi cells are partitions of the variable space based on the distance between data points, described in [64]. The value of $L(x)$ is estimated for all Voronoi cells adjacent to the artificial design, and the maximum value of $L(x)$ is used for the evaluation of the merit value. However, as discussed in [63], the computational cost for calculating the boundaries for the Voronoi cells increase rapidly with increasing number of dimensions. To reduce the complexity of the problem, an analysis is made of the variable impact on the objective functions. This was done by evaluating the radial basis function for the variable values used for the initial set of latin hypercube designs evaluated using CFD, where all but one variable is kept fixed at a time and the response to changing each variable is evaluated. The variables determined to have the largest impact on the function value are used. Typically, a few variables dominate the influence on one of the objective functions and six variables were used here. In Paper IV, the merit value was calculated using the polytropic efficiency as the function value, and three out of ten designs each design loop were used as Lipschitz samples. For the optimizations presented as part of *Section* 5, designs loops were intermediately replaced by Lipschitz sampling, where 5 Lipschitz samples were obtained for each of the two objective functions.

5 Re-design of a low-pressure compression system

THIS section presents the design process of a three-stage compressor as well as a transonic fan utilizing the optimization framework originally developed in [59] and further developed as part of the present work. Tip clearances are included in the computational model, meshed using the multi-block approach discussed in *Section* 3.5.1, and the geometries are considered hydraulically smooth. The optimization objectives are to maximize the polytropic efficiency at the design point and to maximize stability, which is evaluated from the maximum static pressure increase in the stage / fan, see *Section* 2.1.1.

The compression system analyzed in the present study is part of a geared turbo-fan configuration with a high bypass ratio of approximately 15 and a thrust during cruise of approximately 50 kN. The baseline design of the components that are re-designed are part of a low-pressure compression system referred to as daVinki, and the re-designed components are referred to as daVinki 2. The purpose of this exercise is to show the versatility of the developed methodology and to provide a framework for discussing challenges that arise when designing a multi-stage compressor. When optimizing stages that are part of a multi-stage compressor, the location of each stage in the compressor should be considered when specifying the objective function for stability, since the stable operating range will likely be limited by a front stage at a part speed condition, and by a rear stage at design speed as previously discussed in *Section* 2.2 of this thesis. On this basis, the objective function for the first and second stage was set as maximum stability at part speed, while a high stability is favored at design rotational speed for the rear stage.

After re-designing the three-stage compressor and the fan, a steady state simulation is made of the complete low-pressure compression system and the bypass duct.

5.1 Design of a three-stage axial compressor

5.1.1 Methodology

The approach used here is to design the stages in a consecutive manner, first optimizing the first stage and moving on to optimizing the next stage once the first stage design is fixed. The flow field at the exit of the first stage is used as the inlet boundary condition for the next stage. To obtain a realistic boundary condition into the first stage, a simulation was made at the outset of the study of the compressor duct from the splitter (directly downstream of the fan) to aft of the baseline first stage. At the inlet to the compressor duct, a radial variation of total pressure was prescribed representative of the total pressure variation downstream of a transonic fan. A constant total temperature was specified based at the inlet. The approach of designing each stage in isolation neglects the interaction between stages, which will have some impact on the flow field. However, from

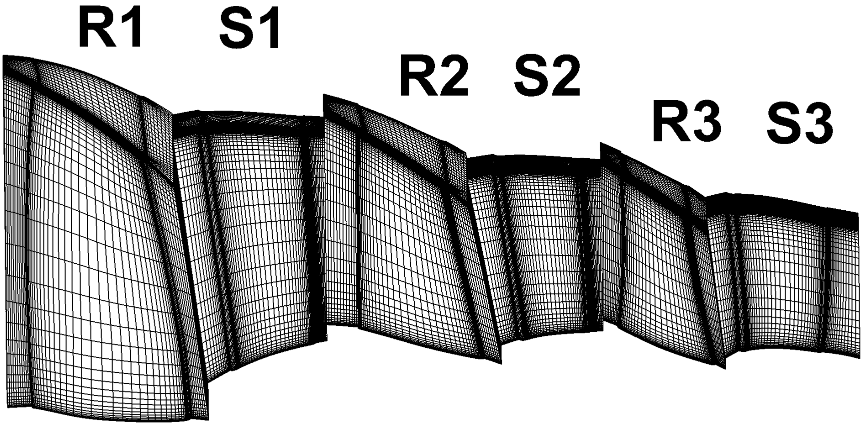

Figure 5.1.1: *Computational grid of the three-stage compressor*

an engineering perspective, if the selected design approach works satisfactory, a significant time gain can be achieved relative to an approach where multiple stages are included in the computational domain.

5.1.2 Computational setup

Baseline design

The baseline design of all compressor blades were provided by GKN Aerospace Engine Systems, and were generated based on data from throughflow calculations. The tip clearance is specified to be the same absolute value for all three rotors. With the blade span decreasing downstream in the compressor, the tip clearance normalized with the rotor span is 0.7%, 1.1% and 1.4% for rotor 1, 2 and 3, respectively at the design point. This choice for the tip clearance size was deemed realistic based on the summary of tip clearance sizes for six different compressor rotors presented in Paper VI, which were in the range 0.4–1.8%. A simplification is made by setting the tip clearance size to be the same at both part and design speed. The relative Mach number in the tip region of the first, second and third rotor is approximately 1.2, 1.2 and 1.0, respectively. The Reynolds numbers (based on the true chord at the tip) are in the range $1.0\text{–}1.3 \cdot 10^6$ the rotors and $3.5\text{–}5.5 \cdot 10^5$ for the stators at design speed. At part speed, the Reynolds numbers are in the range $0.5\text{–}1 \cdot 10^6$ for the rotors and in the range $2\text{–}2.5 \cdot 10^5$ for the stators. The k-ϵ turbulence model with wall functions are used and the flow is considered fully turbulent. The numerical settings are further described in *Section* 3. For all multi-stage simulation results presented in this section, the variation of the outlet boundary condition to find the last stable operating condition was the same. The computational grids for all three stages are shown in Fig. 5.1.1.

Design variables

The design variables are the leading and trailing edge blade angles, as well as a variable impacting the camber distribution along the chord and the stagger angle. The axial chord was kept constant. Furthermore, the number of blades per blade row is included as a design variable. The design variables are altered at three spanwise positions: 0%, 50% and 100% span, making the total number of design variables 10 per blade row.

5.1.3 Results

The Pareto fronts from the optimizations of stages 1, 2 and 3 are shown in Fig. 5.1.2. The maximum efficiency design for each stage is selected, and combined to a three-stage compressor, from here on referred to as daVinki 2.

The corrected mass flow and total pressure ratio for the optimized three-stage compressor, referred to as daVinki 2, is shown at part- and design speed in Fig. 5.1.3a and 5.1.3b, respectively. The corrected mass flow for the compressor was calculated using the total pressure and total temperature at the inlet to the first stage, and corrected to SLS conditions. It is shown that the three-stage compressor can reach the target design point which was specified in an earlier design phase.

ISO-surface of negative axial velocity (-1 m/s) are shown for the compressor operating at design speed in Fig. 5.1.4. In the figure, the blades have been aligned so that the suction surfaces of all blades are visible. A region of negative axial velocity is visible in the tip region of the rotor blades as a result of the tip clearance flow. It is also shown in Fig. 5.1.4a that a separation is present at the design point in the hub region of the second stator (S2). This separation was not present when the second stage was

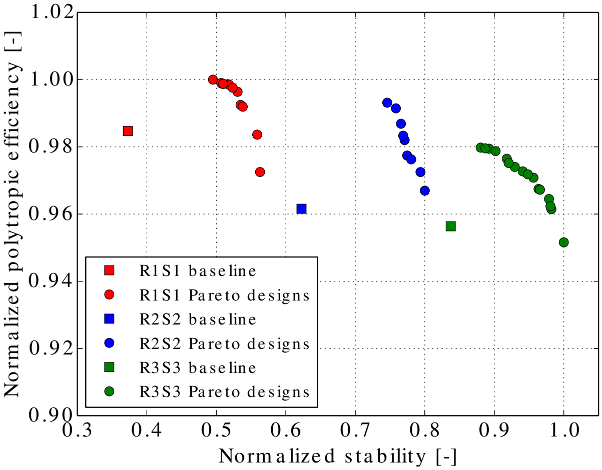

Figure 5.1.2: *Pareto fronts from optimizations of stage 1, 2 and 3*

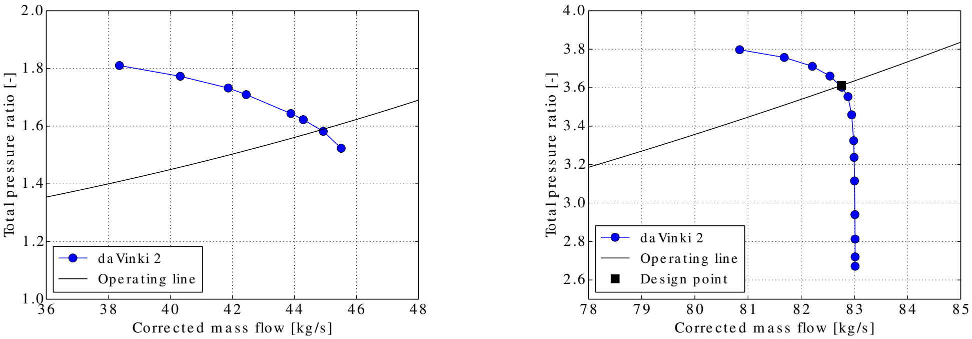

(a) *Part (65%) rotational speed*

(b) *Design rotational speed*

Figure 5.1.3: *Corrected mass flow and total pressure ratio for the three-stage compressor at part and design speed*

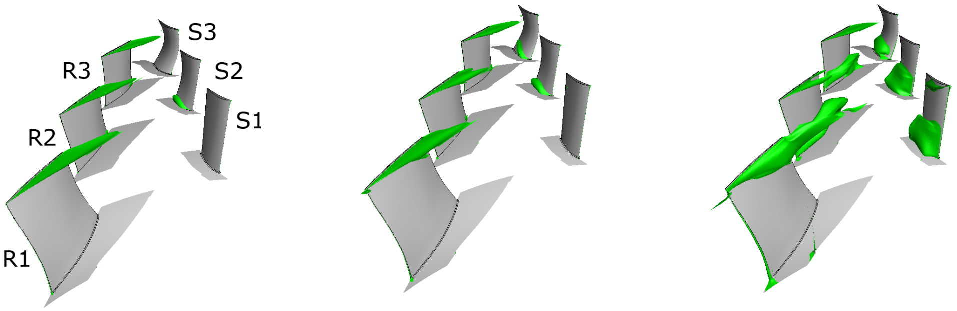

(a) *Design point*

(b) *Last stable operating point*

(c) *Instantaneous solution beyond stall (not converged)*

Figure 5.1.4: *ISO-surfaces of negative axial velocity (-1 m/s) at design speed*

analyzed in isolation or as part of a R1-S1-R2-S2 configuration. It only appears as part of the flow field solution when the downstream stage (R3-S3) is part of the computational domain, showing that the separation is a result of the interaction between the second and third stage. It is shown in Fig. 5.1.4b that as the compressor is throttled to an operating point close to stall, a region of separated flow has also appeared in the hub region of the third stator (S3). Figure 5.1.4c shows iso-surfaces of negative axial velocity for an instantaneous solution for a non-converged solution as the compressor is throttled beyond stall. It is shown that the flow has separated in the hub region of the second and third rotor as well as in the hub region of the stators in all three stages. Relative Mach numbers at 10%, 50% and 90% span for the three-stage compressor (and the downstream strut) at the design point is shown in Fig. 5.1.5. The separation in the hub region of the second stator is visible in Fig. 5.1.5c as a region of low Mach number.

ISO-surfaces of negative axial velocity (-1 m/s) are shown for the compressor operating

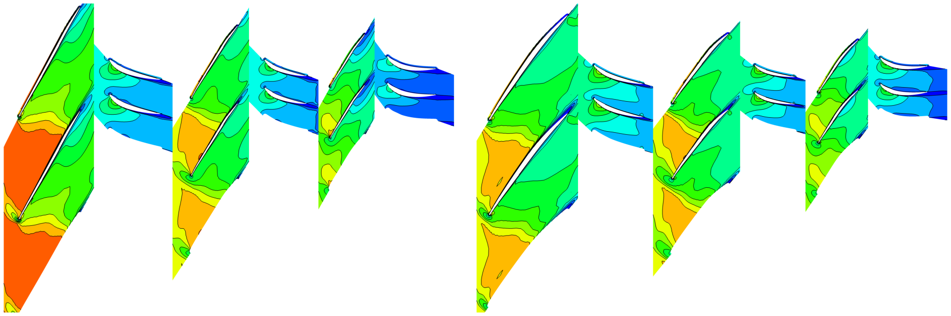

(a) *90% span* **(b)** *50% span*

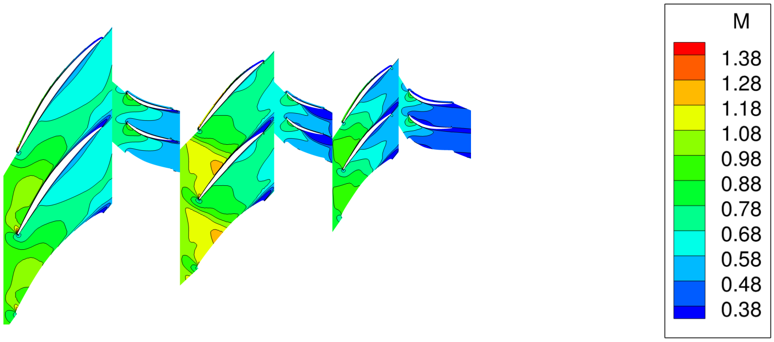

(c) *10% span*

(d) *Legend*

Figure 5.1.5: *Mach number contours at the design point*

at part rotational speed in Fig. 5.1.6. At this operating condition, a low momentum region exist in the hub region at the inlet to the first stage originating from the upstream duct. This low momentum region gives rise to a separation in the hub region of the first rotor, visible for an operating point along the operating line in Fig. 5.1.6a. The size of the separation is shown to increase as the back pressure is increased to an operating point close to stall, see Fig. 5.1.6b. At the operating point close to stall, the flow is also seen to separate on the suction side of the first stator near the hub. As the back pressure is increased even further, no steady state solution could be found and a large number of separated regions are visible in an instantaneous snapshot of the flow field in Fig. 5.1.6c.

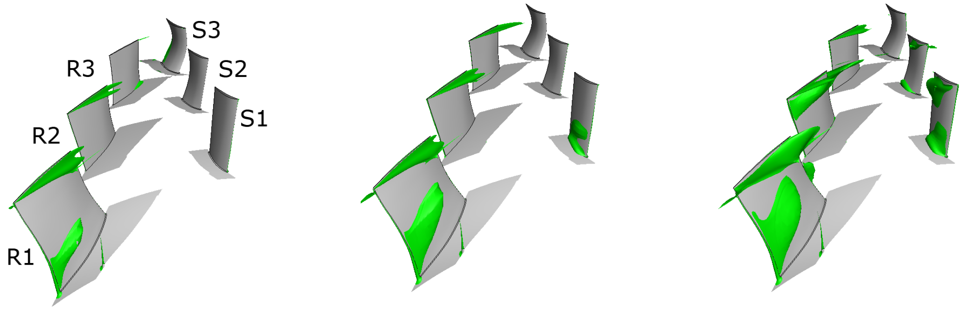

(a) *Operating line* **(b)** *Last stable operating point* **(c)** *Instantaneous solution beyond stall (not converged)*

Figure 5.1.6: *ISO-surfaces of negative axial velocity (-1 m/s) at part speed*

Comparing single stage and multi-stage performance

The performance at design rotational speed of each stage in isolation is compared with the performance of the same stage in the three-stage configuration in Fig. 5.1.7 as the compressor is throttled from choke to stall. The corrected mass flow is calculated using the total pressure and total temperature at the inlet of each stage. It is shown that in isolation, stage 1 in particular, could operate at both a higher total pressure ratio and a lower mass flow compared to the same stage as part of the multi-stage assembly. It is difficult to determine with certainty which stage limits the stable operating range, as several regions of separated flow (previously illustrated in Fig. 5.1.4) grow simultaneously as the back pressure was increased beyond the last stable operating point.

It is shown in Fig 5.1.7 that the polytropic efficiency of the stages is overall lower when considered as part of the multi-stage assembly, relative to the estimation obtained when considered in isolation. Polytropic efficiencies at the design point for stages 1, 2 and 3, normalized with the efficiency for stage 1 in the optimization are shown in table 5.1.1. It is shown that the decrease in polytropic efficiency at the design point when considered as part of the three-stage compressor is similar for all three stages, approximately 0.5%. As the inlet condition to each stage was obtained from a simulation of the upstream stage in isolation, the interaction between the stages was not accounted for which has had an adverse impact on efficiency.

Table 5.1.1: Normalized polytropic efficiencies at the design point

Stage	1	2	3
Single stage sim.	1.000	0.991	0.980
Assembly sim.	0.995	0.987	0.974

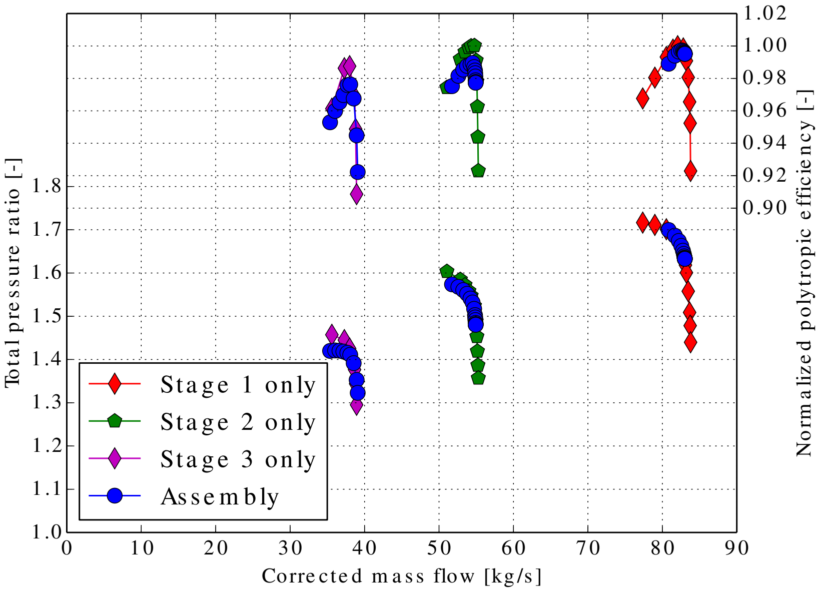

Figure 5.1.7: *Performance at design rotational speed for the stages in isolation and as part of the multi-stage assembly*

The performance is shown for the stages considered in isolation and as part of the three-stage compressor at part speed in Fig. 5.1.8. At part rotational speed, the surge margin of a multi-stage compressor is typically limited by the front stages as previously discussed in *Section* 2.2, and it is seen that the rear stage of this compressor could operate at both lower mass flow and higher total pressure ratio when considered in isolation compared to when it is introduced into the multi-stage environment. As for the design rotational speed, it is difficult to determine which stage stall first as multiple regions of separated flow grow simultaneously as the back pressure was increased beyond the last stable operating point.

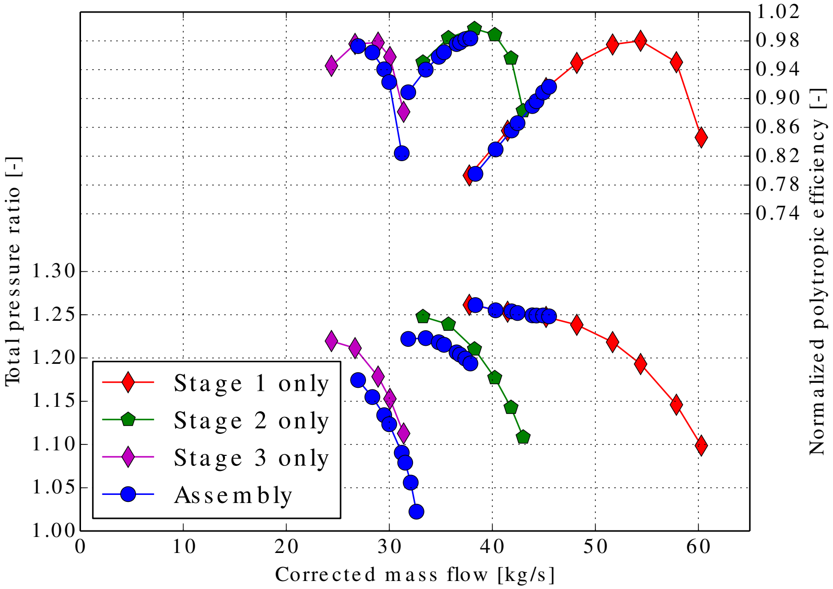

Figure 5.1.8: *Performance at part rotational speed (65%) for the stages in isolation and as part of the multi-stage assembly*

Replacing the front stage

To evaluate the strength of the stability measure used in the optimization, the front stage design is replaced with a high stability design to evaluate if the surge margin of the three-stage compressor is increased at the part-speed condition. The performance of the three-stage compressor before and after replacing the first stage design is shown at part- and design speed in Fig. 5.1.9a. The surge margin is calculated using the expression previously shown in Eq. 2.1.3, and repeated here as Eq. 5.1.1.

$$SM = \left(\frac{PR_{TT,limit} \times \dot{m}_{ref}}{PR_{TT,ref} \times \dot{m}_{limit}} - 1 \right) \times 100 \tag{5.1.1}$$

At part speed, the surge margin for the three-stage compressor has increased from 33% to 36% by using the highest stability design while the surge margin at design speed decreased from 8.4% to 6.7%. It is shown that the design point is still reached for the new compressor design.

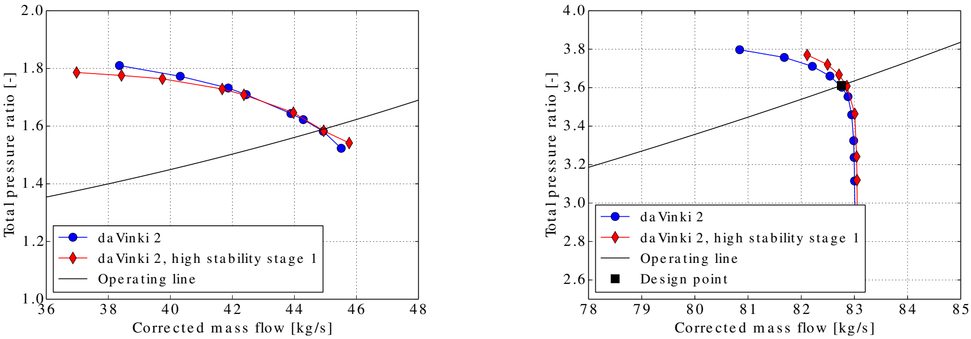

(a) *Part rotational speed*

(b) *Design rotational speed*

Figure 5.1.9: *Corrected mass flow and total pressure ratio for the three-stage compressor with stage 1 replaced with a higher stability design*

Replacing the rear stage

If a higher surge margin is desired for the three-stage compressor at design rotational speed, one approach to achieve this could be to replace the rear stage design. To investigate this, the performance of the three-stage compressor is evaluated when the third stage is replaced with a design in the Pareto front with higher stability. The performance curve for this new three-stage compressor is shown as the green line in Fig 5.1.10. By replacing the rear stage, the estimated surge margin at design speed has increased from 8.4% to 9.2%. Again, it is shown that the design method used in the present study allows for a stage to be replaced and the complete three-stage compressor still reach the design point. For all three compressor configurations shown in Fig. 5.1.10, the total pressure ratio at the design point is reached with a difference in mass flow of ±0.2%.

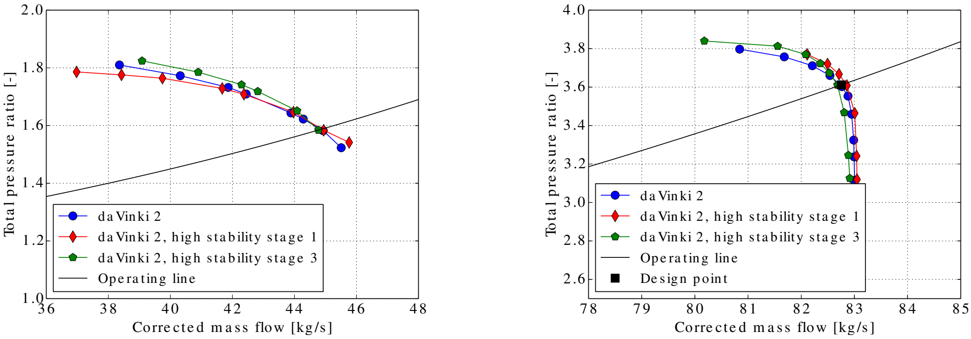

(a) *Part rotational speed*

(b) *Design rotational speed*

Figure 5.1.10: *Corrected mass flow and total pressure ratio for the three-stage compressor with stage 3 replaced with a higher stability design*

5.2 Transonic fan re-designed

The baseline fan blade design was derived from a simplified 2D flow analysis and was provided by GKN Aerospace Engine Systems. The relative Mach number in the tip region is 1.2 and the Reynolds number is approximately $4{\cdot}10^6$ at the design point based on the true chord at the tip. The numerical setup is the same as for the low-pressure compressor

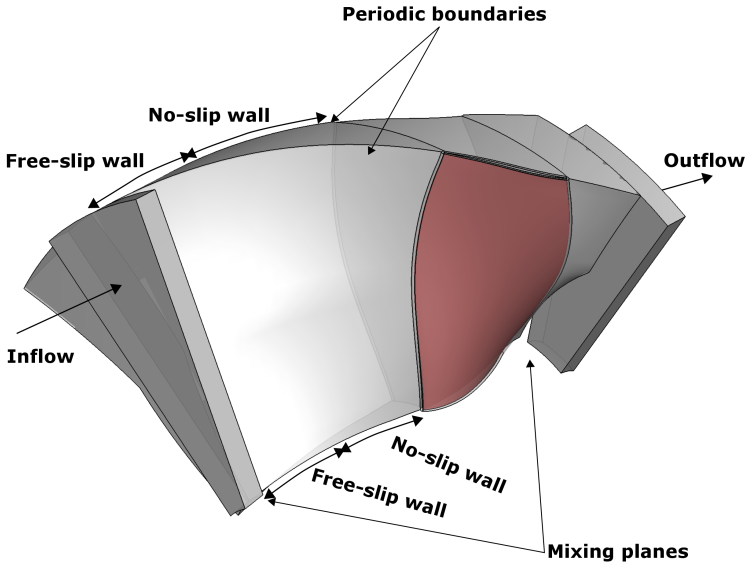
Periodic boundaries
No-slip wall
Free-slip wall
Outflow
Inflow
No-slip wall
Free-slip wall
Mixing planes

Figure 5.1.11: *Compudational domain used for fan design*

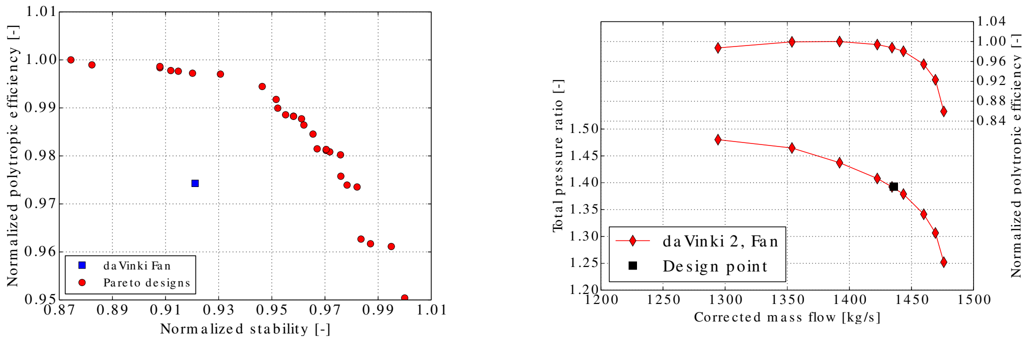

(a) *Pareto front*

(b) *Optimized fan performance*

Figure 5.1.12: *Pareto front and performance of the optimized transonic fan*

described in the previous section and will not be repeated here. The tip clearance is set as 0.5% of the span, the same relative size as for NASA Rotor 35 and 37 [65]. The computational domain is shown in Fig. 5.1.11, and ends in the downstream direction just prior to the splitter. The design variables used in this study are the leading and trailing edge blade angles at three spanwise locations: 0%, 50% and 100% span, resulting in a total of 6 design variables. The Pareto front as well as the performance for a fan blade design design picked from the Pareto front are shown in Fig. 5.1.12. The Pareto front in Fig. 5.1.12a shows that a gain of approximately 2.5% in polytropic efficiency is possible relative to the baseline design. The peak efficiency of the blade design was not impacted to the same extend. Rather, for the optimized designs with high efficiency, the peak efficiency is now closer to the design throttle. The fan design selected from the Pareto front to be analyzed further is the design with a normalized stability of 0.93. Fig. 5.1.12b shows that the design point is indeed reached by the new fan design, now referred to as the daVinki 2 fan. Mach number contours for the optimized blade geometry are shown in Fig. 5.2.1.

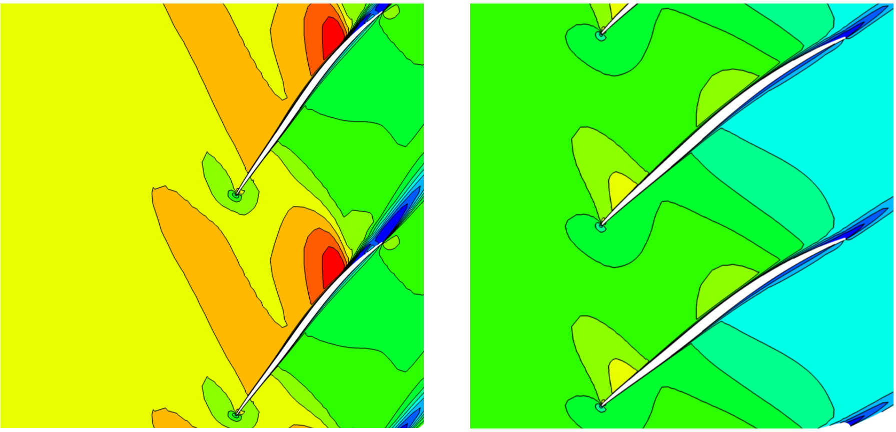

(a) *90% span* **(b)** *50% span*

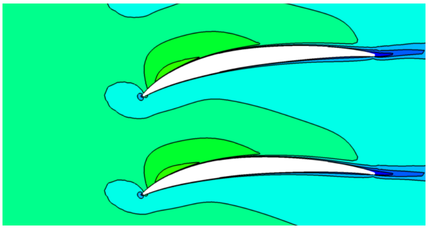

(c) *10% span*

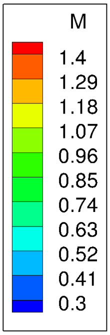

(d) *Legend*

Figure 5.2.1: *Mach number contours at the design point*

5.3 Complete low-pressure compression system

With a new fan blade design obtained from optimization, a steady state simulation is run of the complete low-pressure compression system. Including the bypass duct as well as the core flow means that two outlet boundary conditions are used, and both needs to be varied to find the design point for the fan and the compressor. The corrected mass flow and total pressure ratio of the fan and compressor from this simulation of the complete low-pressure compression system are shown in Fig. 5.3.1a and 5.3.1b. The corrected mass flow for an operating point along the operating line for the compressor is approximately 0.4% higher in the simulation of the complete assembly. The pressure distribution on the walls at the design point is shown in Fig. 5.3.2.

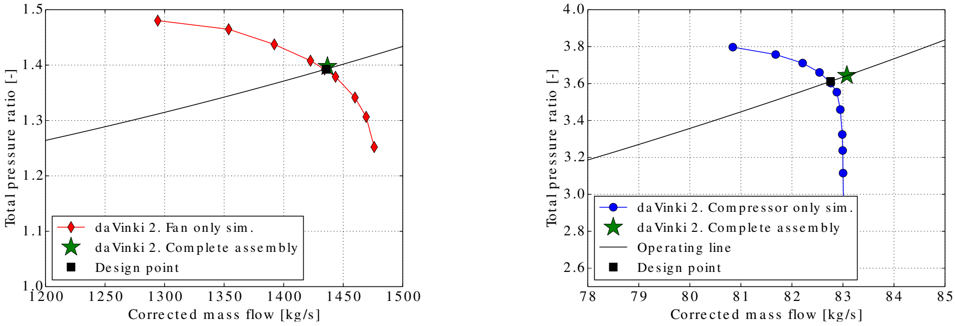

(a) *Fan* **(b)** *Three-stage compressor*

Figure 5.3.1: *Total pressure ratio variation with corrected mass flow*

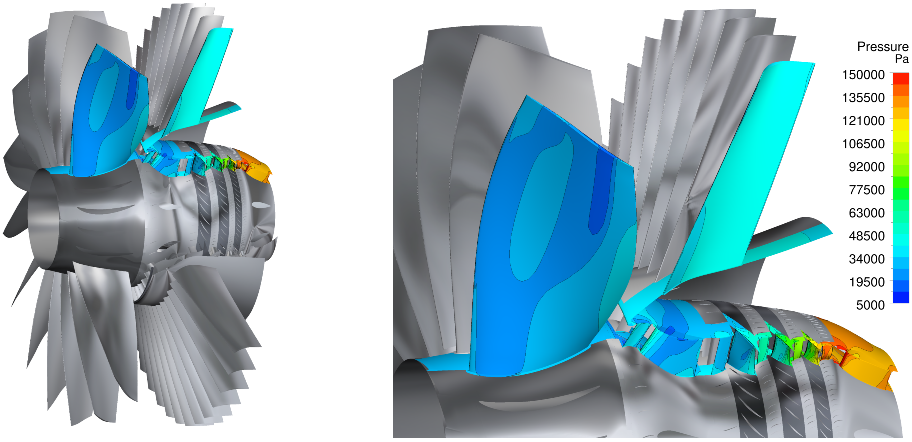

(a) *Static pressure contours* **(b)** *Close-up view*

Figure 5.3.2: *Static pressure field shown for the complete low-pressure compression system*

6 Summary of Papers

6.1 Paper I

M. Lejon, L-E. Eriksson, N. Andersson and L. Ellbrant, 2015, Simulation of Tip-Clearance Effects in a Transonic Compressor, *Proceedings of ASME Turbo Expo 2015*, June 15–19, Montréal, Canada.

6.1.1 Division of work

My contribution, besides being the lead author, was to generate the computational grids, perform the mesh convergence study, setup and run the CFD simulations, and to post-process and interpret the results. Co-authors supervised the work and provided support with regards to analysis of the results and writing of the paper. Co-authors also provided tools for post-processing the results. The geometry and experimental data for the transonic compressor HULDA was provided by GKN Aerospace Engine Systems.

6.1.2 Summary and discussion

This paper compared results obtained using different wall modeling approaches with experimental results for a transonic compressor with a tip clearance of 1.65% of the rotor tip chord. It was shown that the k-ϵ turbulence model using wall functions under-predicted the total pressure ratio of the stage, which was discussed to be in part due to predicting a thicker boundary layer relative to the low-Reynolds model. Using Chien's low-Reynolds model to resolve the boundary layer showed good agreement with experimental data away from stall. It was shown that the variation in polytropic efficiency for a range of mass flows were in good agreement with the experiment using both wall functions and the low-Reynolds model, suggesting that the variation of the dominating loss mechanisms as the compressor is throttled can be captured using the k-ϵ turbulence model and both wall modeling approaches. The surge margin (SM) obtained using the k-ϵ turbulence model and the two wall modeling approachs in this paper were estimated and reported in Paper VI. The SM estimated using wall functions were closer to the experimental value compared to the SM estimated using Chien's low-Reynolds model. Furthermore, the SAS-SST model in ANSYS CFX was used in the study and was shown to predict performance well but required significantly more computational resources. The SAS-SST model was shown to be a good candidate for accurate performance estimation, while using the k-ϵ turbulence model with wall functions could work well for optimization purposes where a large set of designs must be evaluated. Using Chien's low-Reynolds model formulation instead of wall functions could be an appropriate choice to use to evaluate performance at a design point, as it compares well with experimental data away from stall. All models predicted a lower total pressure aft of the rotor close to the hub, which may be due to a separation predicted in the CFD which was not present in the experiment. Uncertainties in the study include measurement uncertainties, the inlet boundary condition and the geometry. A future study focusing on these uncertainties may provide new insights.

6.2 Paper II

M. Lejon, N. Andersson, L. Ellbrant and H. Mårtensson, 2015, CFD Optimization of a Transonic Compressor Stage with a Large Tip Gap, *22nd ISABE Conference*, October 25–30, Phoenix, USA.

6.2.1 Division of work

My contribution, besides being the lead author, was to generate the computational grids, perform a mesh convergence study, setup and run the CFD simulations, perform the optimization, and to post-process and interpret the results. Co-authors supervised the work and provided support with regards to analysis of the results and writing of the paper. Co-authors assisted in setting up the optimization process. The geometry of the baseline compressor stage was provided by GKN Aerospace Engine Systems.

6.2.2 Summary and discussion

Results from two optimizations of a transonic compressor stage were presented in this paper. The first approach did not consider any tip clearance during optimization, and the impact of tip clearance flow on performance was assessed after optimization while the second approach included a tip clearance of 2.5% of the leading edge span in the optimization process. The results were compared in order to discuss the importance of including a tip clearance in the design process. It was concluded that including the tip clearance has an influence on design variables at all radial positions. Redistribution of the flow in the passage has a clear influence on the rotor incidence angle. It was shown that the rotor stagger angle was reduced at lower spanwise positions to allow for a higher mass flow away from the tip region, which is needed to compensate for blockage caused by the tip clearance flow since the designs obtained from the optimizations were all required to reach the specified design point. Designs obtained from the optimization which did not consider any tip clearance flow fail in this respect when evaluated with a tip clearance, as the speed line is shifted to lower mass flow. To confirm that the predicted efficiency using wall functions were consistent with results from a low-Reynolds model, three designs with tip clearances were chosen from a Pareto front and evaluated at the design point using Chien's low-Reynolds model to resolve the boundary layers. The ranking was shown to be the same, although the polytropic efficiency was predicted to be overall lower using the low-Reynolds model.

6.3 Paper III

M. Lejon, N. Andersson, T. Grönstedt, L. Ellbrant and H. Mårtensson, 2016, Optimization of Robust Transonic Compressor Blades, Proceedings of ASME Turbo Expo 2016, June 13-17, Seoul, South Korea.

6.3.1 Division of work

My contribution, besides being the lead author, was to generate the computational grids, perform a mesh convergence study, setup and run the CFD simulations, perform the optimization, and to post-process and interpret the results. Co-authors implemented the surface roughness model in the CFD solver. Furthermore, co-authors supervised the work and provided support with regards to analysis of the results and writing of the paper. The geometry of the baseline compressor stage was provided by GKN Aerospace Engine Systems.

6.3.2 Summary and discussion

The aim of this paper was to determine the importance of including surface roughness in the design phase of a transonic compressor blade. To evaluate this, the optimal design of a compressor stage was analyzed with and without accounting for surface roughness. A modified wall function was used to model the effects of an increased surface roughness on the boundary layers on the blade surfaces. The difference in efficiency for the highest efficiency design from the optimization considering hydraulically smooth walls relative to the highest efficiency design from the optimization considering surface roughness was 0.1% once the blades from the first optimization were subject to surface degradation. The main difference was concluded to be a difference in stagger angle, which allow for the blade optimized considering surface roughness to still reach the design point at design rotational speed. As discussed and demonstrated in the paper, the change in mass flow could be compensated for by an increase in rotational speed. However, as discussed in [66], if the exit temperature from the compression system was already limited by the material then the pressure ratio cannot be regained without exceeding this temperature as the efficiency decrease. A continuation of the study in Paper III was presented in *Section* 3.5.2 of this thesis, where the limit of the design variable range was removed and the optimization was continued. The same conclusions could be made from this extented analysis. The designs obtained from the optimization considering smooth surfaces, once degraded, were essentially a part of the Pareto front obtained from the optimization using rough blades surfaces. The results imply that a the compressor blades can be designed considering smooth blade surfaces. However, as a previously study in [10] showed that surface roughness can cause a separated region to grow in size, it can be good practice to verify that surface roughness for a selected stage design from the Pareto front does not trigger or increase the size of a separation. The computational model used in [10] was similar to that used here in Paper III, *i.e.*, a shift to the law of the wall was made based on the sand grain roughness Reynolds number.

6.4 Paper IV

M. Lejon, T. Grönstedt, N. Glodic, P. Petrie-Repar, M. Genrup, A. Mann, 2017, Multidisciplinary Design of a Three-Stage High Speed Booster, *Proceedings of ASME Turbo Expo 2017*, June 26–30, Charlotte, USA.

6.4.1 Division of work

My contribution, besides being the lead author, was optimizing the compressor blades of the first stage based on performance predictions from 3D CFD calculations. This included generating the computational grids, perform a mesh convergence study, setup and run the CFD simulations, perform the optimization, and to post-process and interpret the results. Co-authors did the preliminary design of the compressor as well as an analysis of the aeromechanical properties of the first stage blade design. Furthermore, co-authors of the paper wrote the sections corresponding to their respective part of the study and provided feedback on the writing of the paper.

6.4.2 Summary and discussion

This paper was written as a result of a collaborative effort between universities in Sweden, showing the joint capability to perform the necessary steps leading to a 3D definition of a high speed compressor. The geometry and boundary conditions needed to run simulations of the compressor presented in this paper were made publically available for anyone to download on a server specified in the paper. The design process, starting from basic aircraft and engine requirements and ending with a 3D geometry of a compressor stage evaluated in terms of its aerodynamic and aeromechanical properties, was described. The first stage was optimized with respect to polytropic efficiency at the design point and surge margin at design rotational speed. The tip clearance size was not set as part of the design work in this paper, but could be evaluated in a future study of the radial displacement of the rotor subject to the design rotational speed, and from considering the thermal expansion of the shroud. Depending on the tip clearance size, additional blockage can result in a different optimal geometry for the compressor blades as shown in Paper II. If a realistic tip clearance is determined to be less than 0.4% of the blade span, it will likely only have a small influence on the flow field as reported in [21–23]. For a larger tip clearance it can become significant to the flow field and the design variables. Results presented in Paper II showed that the difference in polytropic efficiency was heavily influenced (1.6% difference) by the including a rotor tip clearance of 2.5% span in the optimization.

6.5 Paper V

M. Lejon, N. Andersson, T. Grönstedt, L. Ellbrant and H. Mårtensson, 2017, On Improving the Surge Margin of a Tip-Critical Axial Compressor Rotor, *Proceedings of ASME Turbo Expo 2017*, June 26–30, Charlotte, USA.

6.5.1 Division of work

My contribution, besides being the lead author, was to generate the geometries analyzed in the paper, to generate the computational grids, perform a mesh convergence study, setup and run the CFD simulations, perform the optimization, and to post process and interpret the results. Co-authors supervised the work and provided support with regards to analysis of the results and writing of the paper. The baseline rotor geometry was provided by GKN Aerospace Engine Systems.

6.5.2 Summary and discussion

The aim of this paper was to gain more knowledge on how to design a tip-critical rotor for a high surge margin. The investigated rotor geometries were obtained by mainly altering the geometry of a reference rotor in the tip region while ensuring that the design point could still be reached for all designs. When generating the blade geometries, the design space was explored with the aim of finding designs with a high variation in design variables relative to one another. It was found that two different measures could be analyzed at the design point for a tip-critical compressor rotor to determine if it can be expected to have an improved surge margin relative to a different design. At the design point, it was shown to be beneficial with a high incoming axial momentum combined with a low level of loss in the tip region. A tangential force coefficient is defined for the outer 10% of the span, and it is shown to be an equivalent measure to the incoming axial momentum for this evaluation. It is proposed in the paper that to find designs with a high surge margin, an optimization can be done to favor high incoming momentum/tangential force and a low level of loss in the tip region. To verify these proposed objectives, an optimization was done and a design obtained from the optimization was shown to have a high surge margin.

6.6 Paper VI

M. Lejon, N. Andersson, L. Ellbrant and H. Mårtensson, 2017, The Surge Margin of an Axial Compressor: Estimations from Steady State Simulations, *23rd ISABE Conference*, September 3–8, Manchester, UK.

6.6.1 Division of work

My contribution, besides being the lead author, was to perform an extensive literature study and generate CFD results to illustrate methods described in the paper. Co-authors supervised the work and provided feedback on the discussion points and the writing of the paper.

6.6.2 Summary and discussion

This paper reviewed past work where results from steady state calculations have been compared with experimental data. It was noted that as a transient phenomenon, neither surge nor rotating stall can be simulated using steady state simulations of a single blade passage, but the capability of RANS calculations to estimate the surge margin of a compressor is a topic of interest considering the wide use of steady state simulations. The results showed that the surge margin is typically under-estimated using steady state calculations. Furthermore, the paper summarize different approaches that can be used to analyze the stability/surge margin of a compressor rotor or compressor stage.

Advantageous and drawbacks of the different methods were discussed. Work presented as part of this thesis as well as the work of other authors were used for the discussion. It was concluded that maximizing the static pressure increase capability as a weighted average for the both the rotor and stator is an appropriate choice to obtain a compressor stage with high stability. If a single tip-critical rotor is optimized, it was suggested to maximize the incoming axial momentum/tangential force and minimizing the loss generated in the tip region as two objective functions to find designs with a high surge margin. This approach was shown to be successful in finding a compressor rotor design with high surge margin in Paper V.

6.7 Paper VII

M. Lejon, N. Andersson, L. Ellbrant and H. Mårtensson, 2018, The Impact of Manufacturing Variations on Performance of a Transonic Axial Compressor Rotor, *Proceedings of ASME Turbo Expo 2018*, June 11–15, Oslo, Norway. *To be published.*

6.7.1 Division of work

My contribution, besides being the lead author, was to develop the methodology to go from scanned point cloud data of a manufactured blisk to evaluating the impact of manufacturing variations on performance. My contribution was also to generate the computational grids used in the study, to perform the mesh convergence study, setup and run the CFD simulations, to post process and interpret the results. Co-authors supervised the work, provided support with regards to analysis of the results and provided feedback on the writing of the paper. The geometry for the transonic compressor HULDA, the point cloud data of the manufacturing variations and the software used to distort the computational grid were provided by GKN Aerospace Engine Systems.

6.7.2 Summary and discussion

The impact of manufacturing variations on performance and the flow field of a transonic axial compressor rotor was evaluated using steady state CFD simulations considering all blades that make up a rotor blisk. The deviation from design intent for the rotor blades can be divided into two components, a mean deviation and a scatter component around the mean which is unique to each scanned blade. It was shown that the performance shift in terms of mass flow and total pressure ratio was mainly influenced by the mean manufacturing deviation, while the geometric scatter around the mean had a larger impact on the polytropic efficiency. Furthermore, the influence of a single blade deviating significantly from the design intent, denoted as blade 0, as part of a blisk consisting of nominal blades was evaluated. It was shown that a sector of three blades, *i.e.*, blade 0 and a nominal blade on either side, was sufficient to obtain a flow field representative of blade 0 as part of the complete blisk. Using a sector of five blades was shown to be sufficient to obtain a close estimate in the relative change in loss for blade 0 and neighboring blades.

7 Concluding remarks

THE present work has focused on the further development of the optimization framework originally developed as part of [59]. The work has included the selection of an appropriate level of modeling complexity to find compressor stage designs with high stability. An appropriate objective function to find compressor stages with high stability in an optimization has been determined. The current framework allows a rotor or a rotor-stator configuration to be optimized at one or multiple rotational speeds. Surface roughness or the rotor tip clearance can be considered in the computational model. Furthermore, the present work has investigated the impact of surface degradation on optimal compressor design, as well as the impact of manufacturing variations on compressor performance. Multi-stage aspects were considered as a three-stage compressor was designed, starting from baseline blade designs from a design method based on throughflow calculation results. After the three stages were optimized, the performance of the three-stage compressor was evaluated as an assembly. As a final exercise, a transonic fan was optimized and a simulation was run of the complete low-pressure compression system of the geared turbofan engine (fan, bypass duct, outlet guide vane, splitter, inlet guide vanes as well as the three-stage compressor).

7.1 Stability

Different approaches were evaluated as part of the present work to find designs with high stability in an optimization. In Paper II, stage designs were ranked based on the maximum pressure rise capability in the rotor. The maximum static pressure rise capability as a weighted average for the rotor and stator was used in Paper III. In Paper IV, the operating point at which the static pressure increase reached its maximum in either of the blade rows of the stage was found and the operating condition at this point was used to calculate a surge margin. In Paper V, a study was made regarding the surge margin for a tip-critical axial compressor rotor, and two objective functions were proposed to find tip-critical rotor designs with high surge margin.

The conclusion drawn from the studies listed above, which is reflected in Paper VI, is that finding designs with a high static pressure rise capability in both the rotor and stator is an appropriate objective function for optimization purposes of a stage. The measure was consequently used for the the optimization of the three-stage compressor in *Section* 5.1. Unlike the objective functions proposed in Paper V, this measure is more general as it is expected to work well regardless of where a separation occur in a blade passage. As discussed in Paper VI, estimating the maximum pressure rise capability is typically less time consuming than finding the last numerically stable operating point. Finding the last stable operating point may be very time consuming and require a large number of iterations, with the mass flow sometimes showing an asymptotic behavior towards a lower value as iterations progress. Using two objective functions, one reflecting stability and the other efficiency, tradeoffs between the two can readily be made by selecting different designs from a Pareto front.

7.2 Multi-stage optimization

The optimization framework and the selected objective function to reflect stability was used to optimize a three-stage transonic compressor, presented in *Section* 5.1 of this thesis. The location of each stage in the compressor was considered when evaluating stability, as the rotational speed was expected to influence which stage that limit the stable operating range. Each stage was optimized in isolation and, at the end of the optimization of the third and final stage, combined to form a three-stage compressor. The performance of the three-stage compressor was evaluated and verified to reach the target design point. The design approach allowed for the first and third stage designs to be replaced, while still being able to reach the design point for the complete three-stage compressor. By replacing stage designs, a larger surge margin could be achieved at part- or design speed. The study demonstrated the applicability of the objective function used to reflect stability.

7.3 Surface roughness and manufacturing variations

The influence of surface roughness on optimal blade design was evaluated as part of Paper III where it was shown that blades designed without considering surface roughness still perform well once degraded, with similar performance as blades optimized considering surface roughness. It is recommended to optimize compressor blades considering smooth surfaces, and to subsequently evaluate the performance and flow field of selected designs when surface roughness is considered. In Paper III, the increase in boundary layer thickness caused a reduction in mass flow at design rotational speed, which was compensated for by increasing the rotational speed of the compressor and thereby reaching the design point. However, as discussed in [66], if the exit temperature from the compression system is already limited by the material, then the pressure ratio cannot be regained without exceeding this temperature as the efficiency is decreased.

Manufacturing variations were investigated as part of Paper VII, where a methodology was developed and applied for evaluating the impact of manufacturing variations on performance and the flow field of a transonic compressor rotor. In the study, local process capability indices were evaluated on the blade surface, revealing that the largest deviations from a prescribed manufacturing tolerance could be found in the tip region at the leading- and trailing edge. With respect to the impact of manufacturing variations on the flow field, it was shown that the mean deviation from the design intent was mainly responsible for a shift of the speedline, *i.e.* a shift to lower mass flow and lower total pressure ratio. The measured manufacturing scatter around the mean manufactured blade mainly influenced the polytropic efficiency. By analyzing the flow field and radial profiles of total pressure and temperature, it was shown that the main influence of the manufacturing variations for this blisk was in the tip region. The study of a single rotor deviating from the design intent, with nominal rotors on either side, showed that a reduced computational domain can be used and still obtain a representative flow field for the rotor as part of a complete blisk. Analysis such as this may be used to determine more relaxed tolerances that can be allowed for one or a few blades per blisk.

7.4 Future work

Multi-stage optimization should be analyzed further with focus on the interaction of adjacent stages, to potentially improve the performance of the final assembly. Results presented herein showed that a separation in the hub region of the second stage stator was triggered as the third stage was added as part of the computational domain downstream of the second stage. Some uncertainty was connected to deciding the rotational speed at which to evaluate stability for the second stage, where it was decided to evaluate stability at a part speed condition. This choice could be investigated as part of a future study.

Validation of tip-clearance flow prediction capability. It would be of interest to gain further insight on the capability of turbulence models to accurately resolve tip clearance flow. It would also be of interest to perform optimizations using a range of different turbulence models and subsequently evaluate how optimal blade designs were influenced by the choice of turbulence model.

The impact of manufacturing variations for complete blisks could be evaluated using Princical Component Analysis (PCA). Using PCA, a statistical analysis can be made of manufacturing variations using data from measurements, and the information can be used to generate new blade geometries that have some likelihood of being produced. With the ever increase of computational power, evaluating a large number of large computational models is becoming more feasible. The methodology developed as part of the present work to evaluate manufacturing variations was made for a compressor blade without tip clearance, and an extension of this work could be to account for tip clearances.

Bibliography

[1] International Civil Aviation Organization, 2016. ICAO Long-Term Traffic Forecasts: Passenger and Cargo.

[2] International Energy Agency, 2017. Key world energy statistics.

[3] Air Transport Action Group, 2010. ATAG Beginner's Guide to Aviation Efficiency.

[4] Rolls-Royce. Rolls-royce trent 900 turbofan engine. `https://www.rolls-royce.com/products-and-services/civil-aerospace/airlines/trent-900.aspx`. March, 2018.

[5] Pratt & Whitney. Purepower engine family specs chart. `https://www.pw.utc.com/Content/PurePowerPW1000G_Engine/pdf/B-1-1_PurePowerEngineFamily_SpecsChart.pdf`. May, 2018.

[6] Daly, M., 2011. *Janes Aero Engines, Issue 30.* Coulsdon: Jane's Information Group. ISSN: 1748-2534.

[7] Saravanamuttoo, H., Rogers, G., Cohen, H., and Straznicky, P., 2009. *Gas Turbine Theory*, 6 ed. Pearson Education Limited.

[8] Cumpsty, N., 2004. *Compressor Aerodynamics.* Krieger Publishing Company.

[9] Reid, L., and Moore, R. D., 1978. Performance of a single-stage axial-flow transonic compressor with rotor and stator aspect ratios of 1.19 and 1.26, respectively, and with design pressure ratio of 1.82. NASA Technical Paper 1338.

[10] Gbadebo, S. A., Hynes, T. P., and Cumpsty, N. A., 2004. "Influence of Surface Roughness on Three-Dimensional Separation in Axial Compressors". *Journal of Turbomachinery,* ***126***(4), pp. 491–505.

[11] Copenhaver, W., Mayhew, E. R., Hah, C., and Wadia, A., 1996. "The Effect of Tip Clearance on a Swept Transonic Compressor Rotor". *Journal of Turbomachinery,* ***118***, April, pp. 230–239.

[12] Koch, C., 1981. "Stalling Pressure Rise Capability of Axial Flow Compressor Stages". *Journal of Engineering for Power,* ***103***(4), pp. 645–656.

[13] Andersson, J. D., 2003. *Modern Compressible flow: with historical perspective.* McGraw-Hill. ISBN: 978-0-071-12161-3.

[14] Andersson, N., 2005. "A Study of Subsonic Turbulent Jets and Their Radiated Sound Using Large-Eddy Simulation". PhD thesis, Chalmers University of Technology.

[15] Jameson, A., and Baker, T., 1983. "Solution of the euler equations for complex configurations". In In Proceedings of 6th AIAA Computational Fluid Dynamics Conference, no. AIAA Paper 83-1929.

[16] Eriksson, L.-E., 1985. “Practical Three-Dimensional Mesh Generation Using Transfinite Interpolation”. *SIAM Journal on Scientific and Statistical Computing,* ***6***(3), pp. 712–741.

[17] Engquist, B., and Majda, A., 1977. “Absorbing Boundary Conditions for the Numerical Simulation of Waves”. *Mathematics of Computation,* ***31***(139), pp. 629–651.

[18] Stridh, M., 2006. “Modeling Unsteady Flow Effects in 3D Throughflow Calculations”. PhD thesis, Chalmers University of Technology.

[19] Van Zante, D. E., Adamczyk, J. J., Strazisar, A. J., and Okiishi, T. H., 2002. “Wake Recovery Performance Benefit in a High-Speed Axial Compressor”. *Journal of Turbomachinery,* ***124***(2), pp. 275–284.

[20] Denton, J. D., 2010. “Some Limitations of Turbomachinery CFD”. In Proceedings of ASME Turbo Expo 2013: Power for Land, Sea and Air, no. GT2010-22540.

[21] Sakulkaew, S., Tan, C., Donahoo, E., Cornelius, C., and Montgomery, M., 2013. “Compressor Efficiency Variation With Rotor Tip Gap From Vanishing to Large Clearance”. *Journal of Turbomachinery,* ***135***(3), May, p. 031030.

[22] Ellbrant, L., Eriksson, L.-E., and Mårtensson, H., 2011. “CFD Validation of a High Speed Transonic 3.5 Stage Axial Compressor”. In Proceedings of ISABE 2011, no. ISABE-2011-1226.

[23] Ellbrant, L., Eriksson, L.-E., and Mårtensson, H., 2014. “Predictive Capability of CFD Models for Transonic Compressor Design”. In Proceedings of ASME Turbo Expo 2014, no. GT2014-27019.

[24] Storer, J., and Cumpsty, N., 1991. “Tip Leakage Flow in Axial Compressors”. *Journal of Turbomachinery,* ***113***(2), April, pp. 252–259.

[25] Glanville, J. P., 2001. “Investigation into Core Compressor Tip Leakage Modelling Techniques using a 3D Viscous Solver”. In Proceedings of ASME Turbo Expo 2001.

[26] Vo, H. D., Tan, C. S., and Greitzer, E. M., 2008. “Criteria for Spike Initiated Rotating Stall”. *Journal of Turbomachinery,* ***130***(1), p. 011023.

[27] Hah, C., Bergner, J., and Schiffer, H.-P., 2006. “Short Length-Scale Rotating Stall Inception in a Transonic Axial Compressor - Criteria and Mechanisms”. In Proceedings of ASME Turbo Expo 2006, no. GT2006-90045.

[28] McDougall, N. M., 1990. “A comparison between the design point and near-stall performance of an axial compressor”. *Journal of Turbomachinery,* ***112***(1), January, pp. 109–115.

[29] Hewkin-Smith, M., Pullan, G., Grimshaw, S., Greitzer, E., and Spakovszky, Z., 2017. “The Role of Tip Leakage Flow in Spike-Type Rotating Stall Inception”. In Proceedings of ASME Turbo Expo 2017, no. GT2017-63655.

[30] Adamczyk, J., Celestina, M. L., and Greitzer, E., 1993. "The Role of Tip Clearance in High-Speed Fan Stall". *Journal of Turbomachinery,* ***115***(1), January, pp. 28–38.

[31] Suder, K. L., and Celestina, M., 1996. "Experimental and Computational Investigation of the Tip Clearance Flow in a Transonic Axial Compressor Rotor". *Journal of turbomachinery,* ***118***, pp. 218–229.

[32] Van Zante, D. E., Strazisar, A. J., Wood, J. R., Hathaway, M. D., and Okiishi, T. H., 2000. "Recommendations for Achieving Accurate Numerical Simulation of Tip Clearance Flows in Transonic Compressor Rotors". *Journal of Turbomachinery,* ***122***(4), October, pp. 733–742.

[33] Merz, L., Dailey, L., and Orwkis, P., 2004. "A CFD Study of the Flow Through a Transonic Compressor Rotor with Large Tip Clearance". In 40th AIAA/ASME/SAE/ASEE Joint Propulsion Conference and Exhibit, no. AIAA Paper 2004-3934.

[34] Williams, R., Gregory-Smith, D., and He, L., 2006. "A Study of Large Tip Clearance Flows in an Axial Compressor Blade Row". In Proceedings of ASME Turbo Expo 2006: Power for Land, Sea and Air, no. GT2006-90463.

[35] Williams, R., Gregory-Smith, D., He, L., and Ingram, G., 2010. "Experiments and Computations on Large Tip Clearance Effects in a Linear Cascade". *Journal of Turbomachinery,* ***132***(2), January, p. 021018.

[36] Du, J., Lin, F., Chen, J., Nie, C., and Biela, C., 2013. "Flow Structures in the Tip Region for a Transonic Compressor Rotor". *Journal of Turbomachinery,* ***135***(3), May, p. 031012.

[37] Cameron, J. D., Bennington, M. A., Ross, M. H., Morris, S. C., Du, J., Lin, F., and Chen, J., 2013. "The Influence of Tip Clearance Momentum Flux on Stall Inception in a High-Speed Axial Compressor". *Journal of Turbomachinery,* ***135***(6), September, p. 051005.

[38] Cornelius, C., Biesinger, T., Galpin, P., and Braune, A., 2014. "Experimental and Computational Analysis of a Multistage Axial Compressor Including Stall Prediction by Steady and Transient CFD Methods". *Journal of Turbomachinery,* ***136***, June, p. 061013.

[39] Gupta, A., Arif Khalid, S., McNulty, S. G., and Dailey, L., 2003. "Prediction of Low Speed Compressor Rotor Flowfields with Large Tip Clearances". In Proceedings of ASME Turbo Expo 2003, no. GT2003-38637.

[40] Suder, K. L., Chima, R. V., Strazisar, A. J., and Roberts, W., 1995. "The Effect of Adding Roughness and Thickness to a Transonic Axial Compressor Rotor". *Journal of Turbomachinery,* ***117***(4), pp. 455–463.

[41] Bons, J. P., 2010. "A Review of Surface Roughness Effects in Gas Turbines". *Journal of Turbomachinery,* ***132***(2), p. 021004.

[42] Adams, T., Grant, C., and Watson, H., 2012. “A Simple Algorithm to Relate Measured Surface Roughness to Equivalent Sand-grain Roughness”. *International Journal of Mechanical Engineering and Mechatronics,* ***1***(1), pp. 66–71.

[43] Nikuradse, J., 1933. “Ströungsgesetze in rauhen rohren”. *Forschungsheft, Verein Deutscher Ingenieure,* ***361***.

[44] Nikuradse, J., 1950. “Laws of Flow in Rough Pipes, NACA Technical Memorandum 1292”.

[45] Bons, J., 2010. “A review of surface roughness effects in gas turbines”. *Journal of Turbomachinery,* ***132***(2), April, p. 021004.

[46] Goodhand, M. N., Walton, K., Blunt, L., Lung, H. W., Miller, R. J., and Marsden, R., 2015. “The Limitations of Using R_A to Describe Surface Roughness”. In Proceedings of ASME Turbo Expo 2015, no. GT2015-43329.

[47] ANSYS Fluent User’s Guide Version 15.0, ANSYS Inc. 2014.

[48] Bradshaw, P., and Cebeci, T., 1977. *Momentum Transfer in Boundary Layers.* Hemisphere Publishing Corporation.

[49] Koch, C., and Smith, Jr., L. H., 1976. “Loss Sources and Magnitudes in Axial-Flow Compressors”. *Journal of Engineering for Power,* ***98***(3), pp. 411–424.

[50] Garzon, V. E., and Darmofal, D. L., 2003. “Impact of Geometric Variability on Axial Compressor Performance”. *Journal of Turbomachinery,* ***125***(4), pp. 692–703.

[51] Goodhand, M. N., Miller, R. J., and Lung, H. W., 2015. “The Impact of Geometric Variation on Compressor Two-Dimensional Incidence Range”. *Journal of Turbomachinery,* ***137***(2), p. 021007.

[52] Dow, E. A., and Wang, Q., 2015. “The Implications of Tolerance Optimization on Compressor Blade Design”. *Journal of Turbomachinery,* ***137***(10), p. 101008.

[53] Chien, K.-Y., 1982. “Predictions of Channel and Boundary-Layer Flows with a Low-Reynolds-Number Turbulence Model”. *AIAA Journal,* ***20***(1), pp. 33–38.

[54] Liu, Y., Yu, X., and Liu, B., 2008. “Turbulence Models Assessment for Large-Scale Tip Vortices in an Axial Compressor Rotor”. *Journal of Propulsion and Power,* ***24***(1), pp. 15–25.

[55] Menter, F., 1994. “Two-Equation Eddy-Viscosity Turbulence Models for Engineering Applications”. *AIAA Journal,* ***32***(8), pp. 1598–1605.

[56] Launder, B. E., Reece, G. J., and Rodi, W., 1975. “Progress in the Development of a Reynolds-Stress Turbulence Closure”. *Journal of Fluid Mechanics,* ***68***(3), pp. 537–566.

[57] Launder, B. E., and Saplding, D. B., 1972. Lectures in Mathematical Models of Turbulence. Academic Press, London.

[58] Deb, K., Pratap, A., Agarwal, S., and Meyarivan, T., 2000. A Fast and Elitist Multi-Objective Genetic Algorithm: NSGA-II. Tech. rep., Indian Institute of Technology Kanpur. KanGAL Report No. 200001.

[59] Ellbrant, L., 2014. "Multi-objective CFD-based Design Method for Axial Compressors". PhD thesis, Chalmers University of Technology.

[60] Ellbrant, L., Eriksson, L.-E., and Mårtensson, H., 2012. "CFD Optimization of a Transonic Compressor using Multiobjective GA and Metamodels". In 28th International congress of the aeronautical sciences, no. ICAS2012-4.6.3.

[61] Montero Villar, G. "Aerodynamic optimization of high speed propellers". Master's thesis, Chalmers University of Technology.

[62] Alvarez, L. F., 2000. "Design Optimization Based on Genetic Programming". PhD thesis, University of Bradford.

[63] Lovison, A., 2010. "Adaptive Sampling with a Lipschitz Criterion for Accurate Metamodeling". *Communications in Applied and Industrial Mathematics,* ***1***(2), pp. 110–126.

[64] Klein, R., 2011. *Concrete and Abstract Voronoi Diagrams.* Springer. ISBN: 978-3-540-52055-9.

[65] Chima, R., 2009. SWIFT Code Assessment for Two Similar Transonic Compressors. 2009 AIAA 2009-1058.

[66] Smith, Jr., L. H., 2001. Compressor Aero Design at General Electric before CFD. ISABE-2001-1002.